Journal of Non-Newtonian Fluid Mechanics 350 (2026) 105649

Contents lists available at ScienceDirect

Journal of Non-Newtonian Fluid Mechanics

journal homepage: www.elsevier.com/locate/jnnfm

Full length article

Droplet deformation and breakup in general planar flows

Michele Giglio *, Giancarlo Esposito, Gaetano D'Avino *, Massimiliano Maria Villone, Pier Luca Maffettone

Dipartimento di Ingegneria Chimica, dei Materiali e della Produzione Industriale, Università di Napoli Federico II, P.le Tecchio 80, 80125 Napoli, Italy

ARTICLE INFO

Keywords:
Maffettone–Minale model
Droplet deformation
Breakup curves
Complex flows
Twin-screw extruder

ABSTRACT

The deformation and breakup of droplets in immiscible liquid–liquid systems are central to predicting blend morphology in industrial mixing flows. In this work, we extend the Maffettone–Minale (MM) model to general planar mixed flows, deriving analytical expressions for droplet deformation and orientation from the steady-state solution of the shape tensor dynamics. Using these results, we formulate generalized breakup curves spanning from purely shear to purely extensional flows. The proposed breakup criterion preserves the functional structure of the MM model while introducing flow-type-dependent parameters calibrated through a combination of experimental data and new direct numerical simulations. The generalized breakup conditions are tested within an existing morphology-evolution framework for a two-dimensional twin-screw extruder configuration, in order to assess the sensitivity of the predicted droplet-size distribution to the adopted breakup criterion. The framework developed here provides a robust, computationally efficient tool for modeling droplet deformation and breakup in complex industrial flows.

1. Introduction

Immiscible liquid–liquid systems are common in many scientific and technological fields such as polymer, food, pharmaceutical, and cosmetic industries, or even medicine. Their relevance is prominent in several processing applications [1–4]. Indeed, polymer compounding and, more generally, the mixing of a dispersed phase within a matrix have been the subject of extensive experimental studies as well as theoretical and numerical modeling [5–9].

The dynamics of a single drop in a suspending phase subjected to an imposed flow field has received considerable attention in fluid mechanics, as the single-droplet configuration is regarded as a valuable model system for gaining insight into dilute blends. Moreover, the single-drop problem is a benchmark from experimental, theoretical, and numerical perspectives. Early efforts focused on Newtonian drops immersed in Newtonian matrices, and Rallison [10] reviewed the theoretical work on this subject, tracing back to Taylor's pioneering contributions [11,12]. This review mainly addresses small-deformation theories, whereas larger drop deformations and drop breakup were reviewed by Stone [13]. Later, a theory describing the small deformation of a non-Newtonian drop immersed in a non-Newtonian matrix was developed [14], followed by numerous experimental and numerical studies. Guido and Greco [15] reviewed the literature concerning the single-drop problem for both Newtonian and non-Newtonian systems (i.e., where at least one of the constituents is non-Newtonian), discussing the use of rheo-optical techniques, numerical investigations of large drop deformation and breakup, and theoretical advances in small-deformation theories. In addition to exact theories, the problem has been also approached numerically, and Cristini and Tan [16] provided a critical review of the various numerical methods employed in this context.

An alternative to exact theories to predict both drop deformation and the complete internal and external fluid dynamics as a function of the applied flow intensity is the use of simplified models, sometimes based on phenomenological assumptions. The most popular models for drop deformation rely on the assumption that drops deform into ellipsoids, and there are some for both Newtonian and non-Newtonian systems, in either unconfined or confined geometries [17].

When studying liquid–liquid dispersions, it is essential to consider that the dispersed phase may undergo multiple topological changes, including breakup and coalescence [18]. Accurately describing the breakup phenomenon of the dispersed phase under flow is crucial for understanding how microstructure evolves during processing. The pioneering work on this topic is due to Grace [19], who first presented comprehensive experimental data on drop breakup in simple homogeneous shear and planar extensional flows. Using ellipsoidal single-drop models, breakup conditions have been also obtained numerically

* Corresponding authors.
E-mail addresses: michele.giglio@unina.it (M. Giglio), giancarlo.esposito@unina.it (G. Esposito), gaetano.davino@unina.it (G. D'Avino), massimiliano.villone@unina.it (M.M. Villone), pierluca.maffettone@unina.it (P.L. Maffettone).

https://doi.org/10.1016/j.jnnfm.2026.105649
Received 15 April 2026; Received in revised form 7 July 2026; Accepted 24 July 2026
Available online 31 July 2026
0377-0257/© 2026 The Authors. Published by Elsevier B.V. This is an open access article under the CC BY-NC-ND license (http://creativecommons.org/licenses/by-nc-nd/4.0/).

[20–23], yielding results in reasonable agreement with experimental observations [19], although subject to limitations of validity and simplifying assumptions. Another interesting approach for determining breakup curves is based on the Taylor analogy [24–26], though its general applicability is limited. Several studies in the literature have reproduced the drop deformation and breakup mechanisms through numerical simulations [16,27,28], trying to catch the shape of the drop very close to the rupture.

The validity of the Grace curves is, however, limited. Indeed, the scenario changes if drops do not start from a spherical shape [29–31], if the imposed flow is non-uniform or non-homogeneous [32], if confinement effects are present [33,34], or if surface active agents are involved [35]. For instance, in industrial applications dealing with emulsified systems, the local flow is not homogeneous, as it consists of a non-linear combination of reference flow types, ranging from purely rotational to purely extensional. Only a few studies have attempted to experimentally clarify and investigate drop deformation and breakup phenomena in complex kinematics, highlighting that the experimental protocol is not easy to execute. Complex fluid dynamics has been reproduced using four-roll [36,37] and two-roll [38] mill flow cells, an eccentric cylinder device [39–41], a concentric cylinder Couette device [42], and a convergent–divergent channel [43]. From these works, it is clear that reproducing in the laboratory a homogeneous flow with a well-defined extensional character (i.e., the relative intensity of strain versus pure rotation) is extremely challenging, due to the onset of hydrodynamic instabilities that can influence droplet dynamics. Even direct numerical simulations struggle to provide a clear interpretation of deformation and breakup in mixed flows [44,45].

Very recent studies have attempted to model the mixing phenomenon in twin-screw extruders through numerical simulations, highlighting the fundamental role of complex fluid dynamics and mixed kinematics in the blending process that determines the morphology of the final product [46–49]. To accurately describe blending/emulsification of two immiscible liquids within industrial equipment, it is essential to properly represent the behavior of the dispersed phase under mixed flows, which are combinations of rotational (non-deforming) and extensional (deforming) flows.

The objective of this study is to develop a framework for predicting droplet deformation and breakup in general planar mixed flows, overcoming the current limitations of breakup criteria that are restricted to simple shear or extensional conditions. Building on the Maffettone–Minale model [20], we derive analytical expressions for droplet shape and orientation applicable to any combination of strain and vorticity, and we formulate generalized breakup curves through a semi-empirical modification that incorporates flow-type dependence. These curves are calibrated using available experimental data and new direct numerical simulations, leading to accurate prediction of the transition between shear-dominated and extension-dominated breakup regimes. It should be emphasized that the proposed correction is not intended as a unified improvement of the Maffettone–Minale model for both deformation and breakup, but as a semi-empirical modification specifically aimed at reproducing breakup conditions in mixed planar flows. Finally, we demonstrate the applicability of the proposed framework by integrating the generalized breakup conditions into a numerical model for morphology evolution in a twin-screw extruder.

2. Maffettone-Minale phenomenological model

The model developed by Maffettone and Minale [20], hereinafter referred to as the MM model, assumes that the shape of a neutrally buoyant Newtonian droplet in an unbounded Newtonian matrix subjected to flow under inertialess conditions is ellipsoidal at all times and its volume is preserved, i.e., it is incompressible. Therefore, the shape of the drop is described by a symmetric, positive definite, second order tensor, $\boldsymbol{S}$, whose eigenvalues represent the squares of the semiaxes of the ellipsoid. The dimensionless form of the evolution equation for $\boldsymbol{S}$ is

$$\frac{d\mathbf{S}}{dt} - \mathrm{Ca}\,(\boldsymbol{\Omega}\cdot\boldsymbol{S} - \boldsymbol{S}\cdot\boldsymbol{\Omega}) = -f_1\,[\boldsymbol{S} - g\,(\boldsymbol{S})\,\boldsymbol{I}] + f_2\mathrm{Ca}(\boldsymbol{D}\cdot\boldsymbol{S} + \boldsymbol{S}\cdot\boldsymbol{D}), \quad (1)$$

where $\boldsymbol{D}$, $\boldsymbol{\Omega}$, and $\boldsymbol{I}$ are the rate-of-deformation, vorticity, and identity tensors, Ca is the capillary number, and f_1, f_2, and $g(\boldsymbol{S})$ are functions specified below.

According to the MM model, the drop deforms under the competing actions of the drag exerted by the fluid motion and the shape-restoring force related to the interfacial tension between the two immiscible phases. For a system with matching fluid densities, the only two dimensionless parameters that play a role in 'slow' flows (namely, with no inertial effects) are the viscosity ratio, $\lambda = \eta_\mathrm{d}/\eta_\mathrm{m}$, where η_d is the viscosity of the drop and η_m the viscosity of the matrix, and the ratio of the viscous to the interfacial stress given by the capillary number, $\mathrm{Ca} = \eta_\mathrm{m} R_0 G/\sigma$, where R_0 is the radius of the undistorted spherical droplet, G is the macroscopic flow intensity, and σ is the interfacial tension. In Eq. (1) the shape tensor $\boldsymbol{S}$ has been made dimensionless with R_0^2, the time with the characteristic time, $\tau = \eta_\mathrm{m} R_0/\sigma$, and $\boldsymbol{D}$ and $\boldsymbol{\Omega}$ with G. The functions f_1, f_2 and g read

$$f_1 = \frac{40(\lambda+1)}{(3+2\lambda)(16+19\lambda)}, \quad (2)$$

$$f_2 = \frac{5}{3+2\lambda}, \quad (3)$$

$$g = \frac{3III_\mathbf{S}}{III_\mathbf{S}}, \quad (4)$$

where $III_\mathbf{S}$ and $IIII_\mathbf{S}$ are the second and the third invariants of $\boldsymbol{S}$. Notice that a modification of the original f_2 was introduced to better describe the behavior at higher Ca [20], reading

$$f_2^* = \frac{5}{3+2\lambda} + \frac{3\mathrm{Ca}^2}{2+6\mathrm{Ca}^{2+\delta}}\frac{1}{1+\epsilon\lambda^2}, \quad (5)$$

where δ and ϵ are small positive numbers. To all practical purposes, when Ca is not too large and λ is different from zero, δ and ϵ are set to zero, thus Eq. (5) simplifies as follows:

$$f_2^* = \frac{5}{3+2\lambda} + \frac{3\mathrm{Ca}^2}{2+6\mathrm{Ca}^2}. \quad (6)$$

The inclusion of the second term allows for a realistic prediction of the viscosity ratio associated with the experimentally observed vertical asymptote for droplet breakup in shear flow. The function g is required to preserve drop volume, whereas the functions f_1 and f_2 have been determined to recover the asymptotic analytical limits for small Ca and for $\lambda \to \infty$ according to Taylor [12], and the affine deformation behavior for $\lambda = 1$ and $\mathrm{Ca} \to \infty$. Finally, notice that the presence of $g(\boldsymbol{S})$ makes Eq. (1) non-linear in $\boldsymbol{S}$.

The MM model has proven effective in predicting single-drop dynamics under both steady-state conditions [20] and transient regimes [50,51], for small to moderate capillary numbers in simple shear and extensional flows [20]. In addition, it has been used in the case of non-viscometric flows both in laminar [46] and in turbulent [52,53] regimes by applying a Lagrangian description of the fluid dynamics. Furthermore, the MM model nicely describes the droplet deformation and orientation also in combined flows [20,39,46]. However, it fails to predict phenomena occurring at high Ca, such as the 'widening effect' [17] and the divergence of the critical capillary number Ca_cr for droplet breakup as λ goes to zero [22]. Indeed, the model assumes the droplet to always keep an ellipsoidal shape, and is, thus, valid only at $\mathrm{Ca} < \mathrm{Ca}_\mathrm{cr}$ and cannot be expected to accurately predict large deformations and breakup behavior.

3. Generalized Taylor deformation parameter and droplet orientation

In this section, we derive analytical expressions for the Taylor deformation parameter and the droplet orientation in a general planar flow field, without any assumption on the parameters f_1 and f_2 except that they must be independent of $\boldsymbol{S}$. Analytical results conceptually related to those presented here were reported by Boonen et al. [54], who investigated droplet dynamics in mixed flows associated with an eccentric-cylinder device. Their formulation is well suited to the specific flow configuration considered in that work and mainly addresses transient droplet dynamics.

The objective of the present study is different. Here, we focus on steady homogeneous planar linear flows in order to derive generalized breakup conditions extending the classical Grace-type description from shear and planar extension to arbitrary planar mixed kinematics. For this purpose, we adopt the four-roll-mill formulation of Bentley and Leal [37], which provides a direct parametrization of two-dimensional homogeneous flows continuously spanning from rigid-body rotation to simple shear and planar extension. This representation is particularly convenient for distinguishing elliptic and hyperbolic flow topologies and for identifying breakup conditions as a function of the relative strength of strain and vorticity.

Although the formulation of Boonen et al. [54] is fully appropriate for the eccentric-cylinder configuration examined in their study, it is not directly equivalent to the planar mixed-flow family adopted here. In particular, the flow parameter employed in that work, denoted as $\bar{\alpha}$, arises from the generalized velocity gradient associated with the eccentric-cylinder geometry and is therefore closely linked to that specific experimental configuration. For this reason, the Bentley–Leal parametrization is more suitable for the present goal of constructing generalized Grace curves and analyzing breakup in elliptic and hyperbolic planar flows.

As mentioned above, the mixed flow description used in this study follows the approach of Bentley and Leal [36,37]. In their experiments, a four-roll mill device was employed, capable of producing two-dimensional flows with an arbitrary strain-rate-to-vorticity ratio, resulting in the following velocity gradient tensor [36]:

$$\nabla \boldsymbol{u} = \frac{1}{2} G \begin{pmatrix} 1+\alpha & 1-\alpha & 0 \\ -1+\alpha & -1-\alpha & 0 \\ 0 & 0 & 0 \end{pmatrix}, \tag{7}$$

leading to the following dimensionless rate-of-strain and vorticity tensors:

$$\mathbf{D} = \frac{1}{2}\begin{pmatrix} 1+\alpha & 0 & 0 \\ 0 & -1-\alpha & 0 \\ 0 & 0 & 0 \end{pmatrix}, \qquad \boldsymbol{\Omega} = \frac{1}{2}\begin{pmatrix} 0 & 1-\alpha & 0 \\ -1+\alpha & 0 & 0 \\ 0 & 0 & 0 \end{pmatrix}. \tag{8}$$

The flow parameter α is a measure of the relative strength of the strain and vorticity in the flow and ranges from -1, corresponding to purely rotational flow, to $+1$, corresponding to pure straining motion. The value $\alpha = 0$ represents simple shear flow. In Fig. 1, the streamlines corresponding to the general planar linear flows defined above are shown for different values of α.

The ratio between the magnitude of the rate-of-strain tensor, $\| \mathbf{D} \|$, and that of the vorticity tensor, $\| \boldsymbol{\Omega} \|$, can be expressed as

$$\frac{\| \mathbf{D} \|}{\| \boldsymbol{\Omega} \|} = \frac{1+\alpha}{1-\alpha}. \tag{9}$$

From Eq. (9) it is simple to derive

$$\alpha = \frac{\| \mathbf{D} \| - \| \boldsymbol{\Omega} \|}{\| \mathbf{D} \| + \| \boldsymbol{\Omega} \|}. \tag{10}$$

For the homogeneous steady planar flows considered here, Eq. (10) provides a convenient kinematic parameter; in non-homogeneous or unsteady flows it is not objective and must be used with caution, as it will be discussed later.

The steady-state eigenvalues of $\boldsymbol{S}$ obtained by solving Eq. (1) for the generic planar flow defined as in Eqs. (8) read

$$L^2 = \frac{(\alpha-1)^2\mathrm{Ca}^2 + f_1^2 + (\alpha+1)\mathrm{Ca}\, f_2 \sqrt{(\alpha-1)^2\mathrm{Ca}^2 + f_1^2}}{[(\alpha-1)^2\mathrm{Ca}^2 + f_1^2]^{1/3}[f_1^2 + \mathrm{Ca}^2((\alpha-1)^2 - f_2^2(\alpha+1)^2)]^{2/3}}, \tag{11}$$

$$B^2 = \frac{(\alpha-1)^2\mathrm{Ca}^2 + f_1^2 - (\alpha+1)\mathrm{Ca}\, f_2 \sqrt{(\alpha-1)^2\mathrm{Ca}^2 + f_1^2}}{[(\alpha-1)^2\mathrm{Ca}^2 + f_1^2]^{1/3}[f_1^2 + \mathrm{Ca}^2((\alpha-1)^2 - f_2^2(\alpha+1)^2)]^{2/3}}, \tag{12}$$

$$W^2 = \frac{[f_1^2 + \mathrm{Ca}^2((\alpha-1)^2 - f_2^2(\alpha+1)^2)]^{1/3}}{[(\alpha-1)^2\mathrm{Ca}^2 + f_1^2]^{1/3}}. \tag{13}$$

The Taylor deformation parameter $D = (L-B)/(L+B)$, where L and B are the maximum and the minimum semiaxes of the ellipsoid, is given by

$$D = \frac{\sqrt{(\alpha-1)^2\mathrm{Ca}^2 + f_1^2} - \sqrt{(\alpha-1)^2\mathrm{Ca}^2 + f_1^2 - (\alpha+1)^2\mathrm{Ca}^2 f_2^2}}{(\alpha+1)\,\mathrm{Ca}\, f_2}. \tag{14}$$

It can be easily noticed that the expressions provided above degenerate into those proposed by the MM model [20] for simple shear ($\alpha = 0$) and planar hyperbolic flow ($\alpha = 1$).

The generalized orientation of the droplet can be computed according to the eigenvector related to the maximum eigenvalue of the shape tensor, resulting in

$$\theta = -\frac{1}{2}\arctan\left[\frac{(1-\alpha)\mathrm{Ca}}{f_1}\right]. \tag{15}$$

Notice that θ is only function of the flow-type index and f_1, confirming that the prediction of the model is insensitive to the change in the function f_2 [20]. We point out that θ denotes the angle between the ellipsoid major axis and the fixed x-axis. For any α, the vorticity vector aligns with the negative z-direction and the principal axes of the rate-of-strain tensor with the x- and y-directions, thus the flow 'exists' in the xy-plane. The flow direction forms an angle, θ_e, with the x-axis of the fixed reference frame such that [36,37]

$$\sin(2\theta_e) = \frac{\alpha-1}{\alpha+1}. \tag{16}$$

For instance, for a simple shear flow ($\alpha = 0$) at low Ca, $\theta = 0$ and $\theta_e = -\pi/4$, i.e., the drop is oriented with the major axis forming a $\pi/4$-angle with respect to the main flow direction, as predicted by the Taylor's theory.

In the limit of $\lambda \gg 1$, $f_1 \to 20/(19\lambda)$ and $f_2 \to 5/(2\lambda)$, thus Eq. (14) becomes

$$D_{\mathrm{lim}} = \frac{5}{4\lambda}\frac{\alpha+1}{|\alpha-1|}, \tag{17}$$

where D_{lim} is the limit of the steady-state deformation of a very viscous droplet in a general planar flow. For $\alpha = 1$, $D_{\mathrm{lim}} \to \infty$, since no steady-state limit exists as a pure extensional flow can break-up a droplet for any λ. For $\alpha = 0$, $D_{\mathrm{lim}} = 5/(4\lambda)$ and $\theta_{\mathrm{lim}} = \theta_e$, so the Taylor limit for simple shear flow is recovered [12]. For $\alpha = -1$, $D_{\mathrm{lim}} = 0$, since a pure rotational flow cannot deform the droplet.

Below, we present the predictions for the deformation parameter and orientation angle in hyperbolic ($\alpha > 0$) and elliptic ($\alpha < 0$) flows [55]. As also indicated by the original model results [20], the correction proposed for f_2 through Eq. (6) does not systematically lead to significant improvements in the prediction of the deformation parameter when the flow is not shear-dominated. In the case of planar extensional flow, the effect of the correction is almost negligible. This behavior can be attributed to the fact that the proposed function was specifically modified to recover the Grace curve in shear flow by introducing parameters obtained through numerical fitting, effectively treating the breakup in simple shear as the limiting case of droplet behavior. Conversely, the agreement with the Grace curve in extensional flow was only verified *a posteriori* after introducing the shear correction, without implementing additional modifications to the

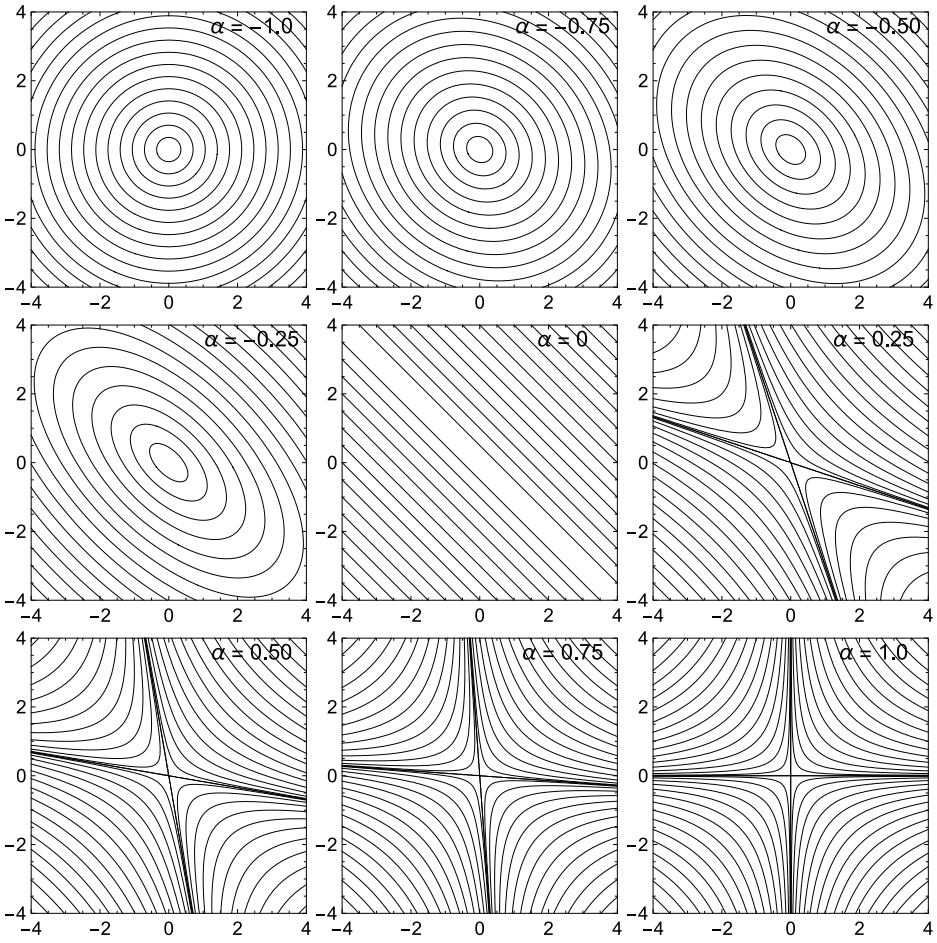

Fig. 1. Streamlines of the flow fields described by Eq. (7) for several values of the flow parameter, α.

model. As a consequence, the resulting formulation becomes highly specialized for shear flow conditions, while the breakup behavior in flows with different topologies is not explicitly accounted for. For this reason, we derive the deformation parameter and the orientation angle in mixed planar flows by using the original formulation of f_2 in Eq. (3).

3.1. Hyperbolic flows

For hyperbolic flows ($\alpha > 0$), experimental data are available for different values of the flow parameter and viscosity ratio [37]. We also carried out direct numerical simulations (DNS) under the same conditions to validate the numerical method (see the Appendix for further details on the numerical procedure). Figs. 2 and 3 report the comparison between experimental data, DNS results and MM model predictions of the Taylor deformation parameter and the droplet orientation angle. A very good quantitative agreement is observed between experiments and simulation results. As expected, the model accurately captures droplet deformation and orientation at relatively low Ca, while deviations emerge at higher values. The Ca-value beyond which the model predictions fail depends on α and λ and is likely related to the transition to non-ellipsoidal droplet shapes.

To provide a comprehensive picture of the influence of the flow field and the viscosity ratio on droplet deformation, we report in Fig. 4 the predictions of D as a function of Ca for several values of $\alpha \geq 0$ (see legend), each panel corresponding to a different λ. In simple shear flow ($\alpha = 0$), the curves are identical to those reported in the original paper [20]. The dependence of D on λ is strongly related to the value of α. Indeed, the curves with a powerful extensional component (α close to 1) weakly depend on λ, since a strong straining flow can always deform the dispersed phase efficiently. At low viscosity ratio, the dispersed phase can be effectively deformed also by weaker hyperbolic flows (low α); in contrast, as the viscosity ratio increases, the dispersed phase can become extremely viscous with respect to the matrix so that weaker hyperbolic flows are no longer able to effectively deform it, resulting in a progressive flattening of the curves at low/medium α.

Fig. 5 reports the orientation angle, $-\theta$, as a function of the capillary number, Ca, for the same values of α and λ as in Fig. 4. When the viscosity ratio increases, the dispersed phase deforms less at $\alpha \to 0$, but it attains a larger orientation angle. This is in good agreement with what has been reported in the literature [20,37] for small deformations from sphericity, i.e., $D \leq 0.2$; then, quantitative deviations from experiments are observed at higher values of the deformation parameter.

3.2. Elliptic flows

To the best of our knowledge, no experimental data are available for elliptic flows. Hence, we carried out numerical simulations to validate the model predictions. Fig. 6 shows the deformation parameter as a function of the capillary number for several elliptic flows and viscosity ratios. The solid lines and the symbols are the MM model predictions and the numerical simulation results, respectively. First of all, the model exhibits good quantitative agreement with the DNS results, even at high capillary numbers. This behavior can be attributed to the rotational component of elliptic flows, which helps maintain an approximately ellipsoidal droplet shape and thereby mitigates the effect of the stretching component.

In general, the deformation parameter stays closer to the spherical condition when the vorticity magnitude increases. Indeed, it can be

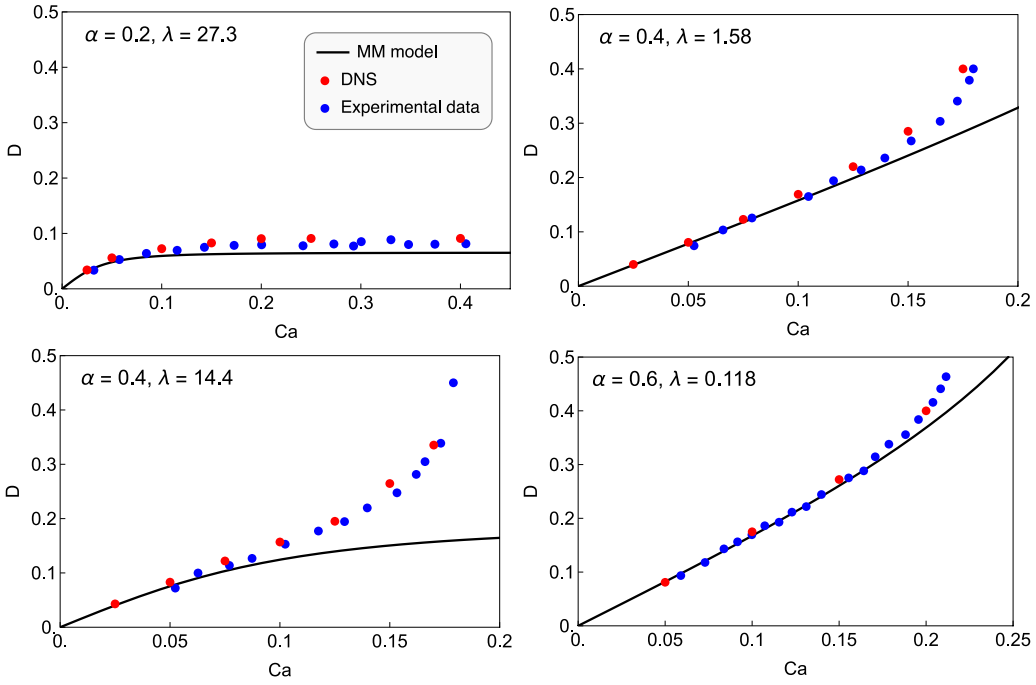

Fig. 2. Taylor deformation parameter, D, as a function of the capillary number, Ca, for different hyperbolic flows and viscosity ratios predicted by the Maffettone–Minale model (lines), our numerical simulations (red circles) and measured by Bentley and Leal [37] (blue circles).

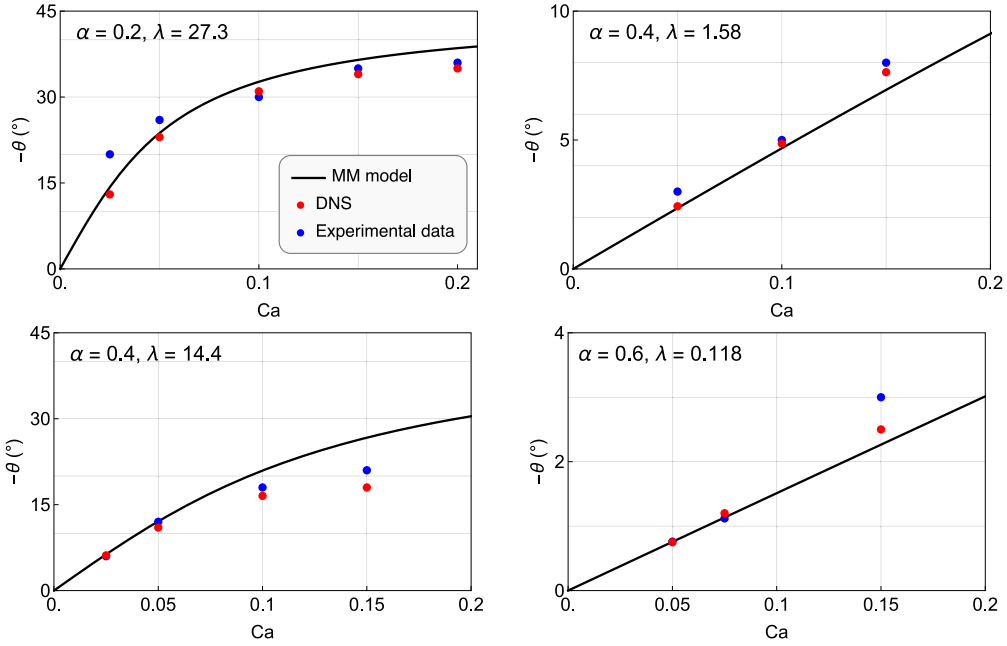

Fig. 3. Orientation angle, θ, as a function of the capillary number, Ca, for different hyperbolic flows and viscosity ratios predicted by the Maffettone–Minale model (lines), our numerical simulations (red circles) and measured by Bentley and Leal [37] (blue circles).

easily proven that, when $\alpha \to -1$, $D \to 0$, meaning that, in a purely rotational flow, the droplet remains spherical, since it behaves as a rigid body. Of course, in strongly elliptic flows, the residual strain components that persist within this type of kinematics do induce some droplet deformation; however, the effect remains very weak.

The model predictions reported in Fig. 7 indicate that, in elliptic flows, the orientation angle depends on the flow index, although this dependence is less pronounced for highly viscous droplets. It is also worth remarking that the angle between the flow direction and the x-axis of the fixed reference frame expressed by Eq. (16) is well defined only for $\alpha \geq 0$, since elliptic flows are characterized by closed streamlines and, thus, lack a univocal flow direction.

4. Generalized grace curves for mixed flows

An important aspect in industrial applications such as polymer blending or emulsion technology is the appropriate description of the breakup phenomenon, required to predict the final droplet size distribution. Modeling works dealing with complex flows roughly estimate the effective critical capillary number for breakup, Ca_{cr}, by means of a flow-type-weighted arithmetic mean between the shear and extensional

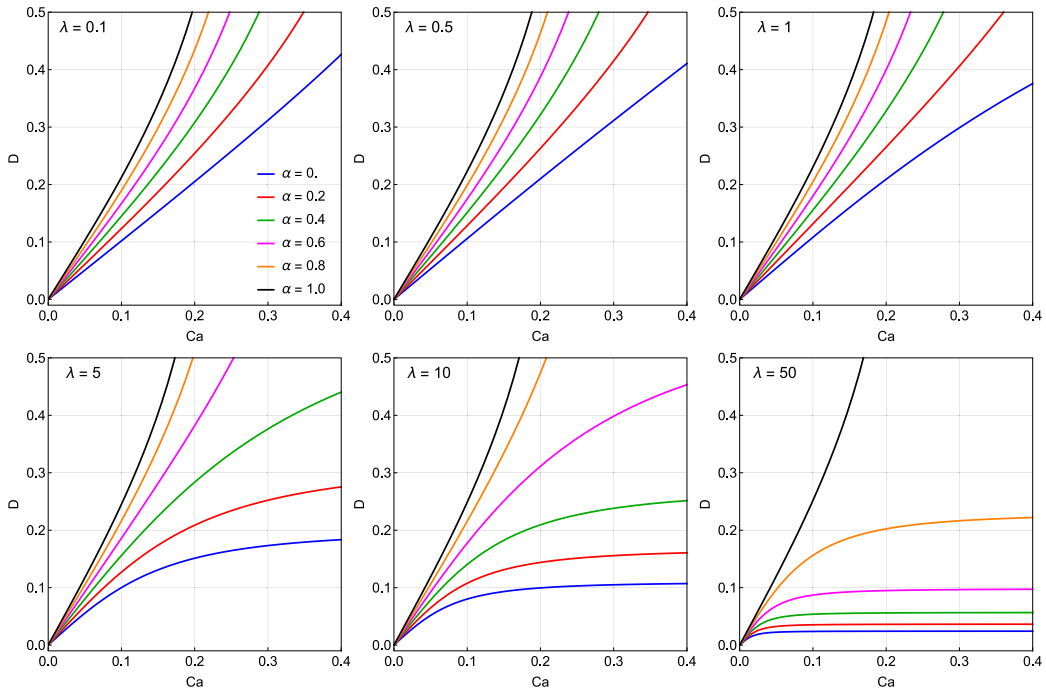

Fig. 4. Taylor deformation parameter, D, as a function of the capillary number, Ca, for several hyperbolic flows ($\alpha \geq 0$, see legend). Each panel corresponds to a different value of the viscosity ratio, λ.

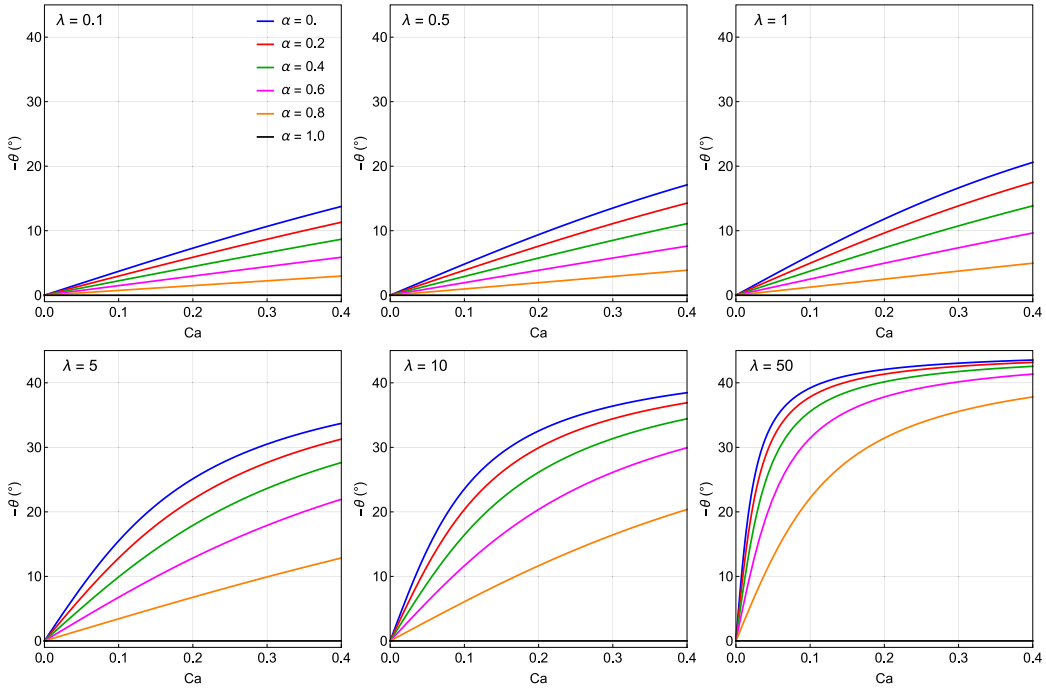

Fig. 5. Orientation angle, $-\theta$, as a function of the capillary number, Ca, for several hyperbolic flows ($\alpha \geq 0$, see legend). Each panel corresponds to a different value of the viscosity ratio, λ.

critical capillary numbers provided by the Grace curves [32,46,56]. However, this heuristic and approximate approach is not applicable when the viscosity ratio exceeds ≈ 3.5, as the critical capillary number in shear flow becomes undefined. Furthermore, no simple usable conditions for breakup are available in the literature when the vorticity magnitude starts overcoming the intensity of the straining ($\alpha < 0$), even if the flow topology is still far to be purely rotational ($\alpha = -1$).

Based on the MM model predictions presented in Section 3, the breakup conditions can be derived in a closed form by observing that, with increasing Ca, the real solution of the steady-state form of Eq. (1) becomes complex at some critical value $\mathrm{Ca} = \mathrm{Ca}_{\mathrm{cr}}$. This can be obtained from the boundary of the real domain of Eq. (14), yielding

$$(\alpha-1)^2\mathrm{Ca}_{\mathrm{cr}}^2 + f_1^2 - (\alpha+1)^2\mathrm{Ca}_{\mathrm{cr}}^2 f_2^2 = 0, \tag{18}$$

which can be re-written as

$$\mathrm{Ca}_{\mathrm{cr}} = \frac{f_1}{\sqrt{(\alpha+1)^2 f_2^2 - (\alpha-1)^2}}. \tag{19}$$

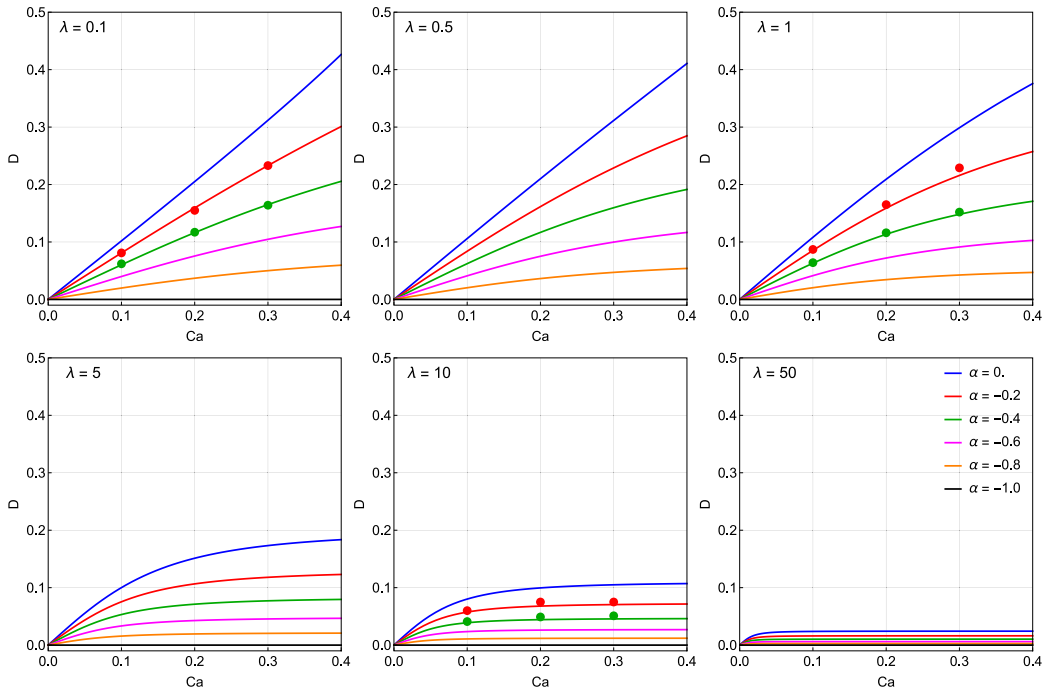

Fig. 6. Taylor deformation parameter, D, as a function of the capillary number, Ca, for several elliptic flows ($\alpha \leq 0$, see legend). Each panel corresponds to a different value of the viscosity ratio, λ. The colored circles represent the results obtained from DNS.

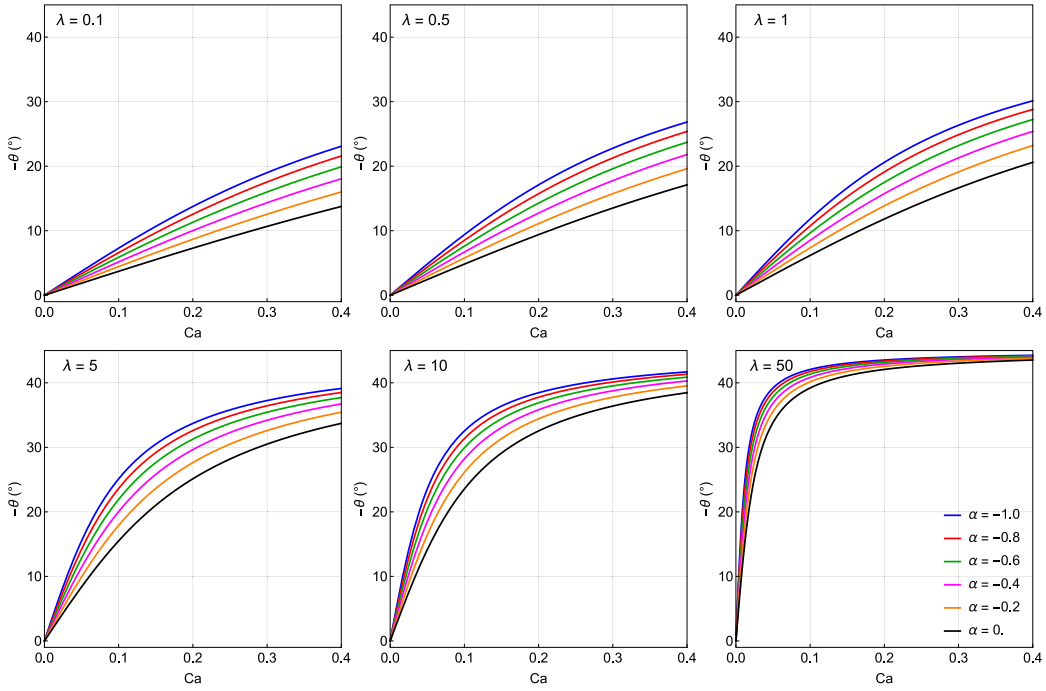

Fig. 7. Orientation angle, $-\theta$, as a function of the capillary number, Ca, for several elliptic flows ($\alpha \leq 0$, see legend). Each panel corresponds to a different value of the viscosity ratio, λ.

Notice that this equation is explicit in $\mathrm{Ca}_{\mathrm{cr}}$ if the original expression for f_2 in Eq. (3) is used, otherwise it becomes implicit in case a Ca-dependence is introduced in f_2 like that in Eq. (6). The function $\mathrm{Ca}_{\mathrm{cr}}(\lambda, \alpha)$ gives the generalization of the Grace curves for any mixed planar flow.

The solution of Eq. (19) by using f_2 in Eq. (3) gives breakup curves with a vertical asymptote in λ for any value of α (except $\alpha = 1$) in disagreement with the experimental evidence [37]. Furthermore, the asymptotic viscosity ratio in shear flow is $\lambda = 1$ which is inconsistent with the Grace curve, as already pointed out in Maffettone and Minale [20]. This is expected as the original expression of f_2 is valid for small capillary numbers, far from the breakup conditions.

We then used the expression of f_2^* in Eq. (6) and numerically solved Eq. (19) for various values of α. The resulting breakup curves were compared with the experimental data of Bentley and Leal [37]. The vertical asymptote in shear flow is correctly captured, as already reported in the original paper [20]. The qualitative trends for $0 < \alpha < 1$ are reproduced as the breakup curves show the asymptote up

to a certain value of α (= 1/3). The quantitative agreement remains unsatisfactory, however, as significant deviations are found between model predictions and both experimental data [37] and our numerical simulations. This outcome is not surprising, since the original function f_2^* was specifically devised to capture breakup behavior in shear flow only.

Despite these quantitative deviations, the overall shape of the predicted curves resembles the experimental trends. For this reason, we decided to preserve the functional structure of f_2^* by replacing the parameters of the second term as functions of α. We considered the following expression for f_2:

$$f_{2,\mathrm{mod}} = \frac{5}{3+2\lambda} + \frac{K_1(\alpha)\mathrm{Ca}^2}{1+K_2(\alpha)\mathrm{Ca}^2}, \tag{20}$$

which recovers f_2^* for $K_1 = 1.5$ and $K_2 = 3$. The functions $K_1(\alpha)$ and $K_2(\alpha)$ have been calibrated by fitting experimental and DNS data. The number of available experimental data points is rather limited because, as the authors emphasize [37], describing the dynamics very close to breakup is extremely challenging because of experimental limitations and the difficulty of achieving sufficient spatio-temporal resolution of the droplet. The critical values of λ are explicitly reported by the authors, but the experimental data themselves are insufficient to perform a meaningful fitting capable of accurately describing the divergences. For this reason, we performed an augmentation of the experimental dataset using a shape-preserving interpolation method, in order to introduce additional points that could support the fitting procedure. The augmentation procedure relies on Piecewise Cubic Hermite Interpolating Polynomials (PCHIP). The augmented data points are introduced only for the cases with $\alpha = 0.2$ and 0.4, corresponding to the configurations in which vertical asymptotes arise at values of λ that cannot be explicitly inferred from the experimental data reported by the authors, although they are stated in the accompanying text [37]. We assessed the sensitivity of the fitted values of K_1 to the fictitious data augmentation by repeating the fitting procedure using only the original experimental data. The resulting values differed by approximately 6% and 3% for $\alpha = 0.2$ and $\alpha = 0.4$, respectively, compared with those obtained when the augmented data were included.

In addition, in order to better characterize the transition region between shear-dominated and extensional-dominated breakup regimes (respectively associated with the presence or absence of a vertical asymptote), we extended the dataset by performing DNS simulations to additional values of α for which experimental data are not available.

To determine the functional forms of K_1 and K_2, we distinguish between flow conditions that exhibit a vertical asymptote in the breakup curve (shear-like behavior) and those that do not (extensional-like behavior). The four-roll-mill experiments of Bentley and Leal [37] show that, for planar hyperbolic flows with $\alpha \leq 0.4$, the breakup curves retain a shear-like character, displaying critical viscosity ratios at which $\mathrm{Ca}_{\mathrm{cr}}$ diverges. The authors explicitly report these asymptotic values for $\alpha = 0.2$ and $\alpha = 0.4$, corresponding to $\lambda = 27$ and $\lambda = 57$, respectively. In contrast, when $\alpha \geq 0.6$, the breakup curves flatten and closely resemble those of pure extensional flow. This transition occurs because a sufficiently strong straining component overwhelms the stabilizing effect of vorticity, promoting breakup for any value of λ. Conversely, when the vortical contribution remains significant, the flow is no longer capable of breaking highly viscous droplets, leading to the appearance of vertical asymptotes in the breakup curves.

In cases where a vertical asymptote is present, i.e., for $\lambda \to \lambda_{\mathrm{asymp}}$, the critical capillary number diverges and $f_{2,\mathrm{mod}}$ reads:

$$f_{2,\mathrm{mod}} = \frac{5}{3+2\lambda_{\mathrm{asymp}}} + \frac{K_1(\alpha)}{K_2(\alpha)}, \tag{21}$$

Hence, Eq. (18) becomes:

$$(\alpha+1)^2\left[\frac{5}{3+2\lambda_{\mathrm{asymp}}} + \frac{K_1(\alpha)}{K_2(\alpha)}\right]^2 - (\alpha-1)^2 = 0. \tag{22}$$

which fixes the ratio K_1/K_2 for a given λ_{asymp} and α. Consequently, the fitting procedure involves only the function $K_1(\alpha)$. Since the data are available at discrete values of α, we performed separate fittings for each α. The parameter K_1 was estimated by minimizing a weighted least-squares objective function. For each data point, the residual was computed as the difference between the measured/simulated capillary number and the value predicted by the theoretical model, i.e., the right-hand side of Eq. (19). This residual was weighted by a factor $1/\mathrm{Ca}_{\mathrm{cr}}^2$, in order to account for the different scales of the capillary number values. The objective function was defined as the sum of the squared weighted residuals over the full data set, with the addition of a quadratic regularization term to stabilize the minimization algorithm. To avoid numerical instabilities associated with the square root appearing in the model, a lower threshold was imposed on its argument. If this argument became smaller than the prescribed threshold, the corresponding residual was replaced by a real penalty term, thus preventing the generation of complex values during the optimization. The minimization was performed using the constrained derivative-free Nelder–Mead algorithm.

The resulting K_1 and K_2 functions are shown in the left side of Fig. 8. The numerical values are reported in Table 1. Notice that the values for $\alpha = 0$ correspond to the functional form of f_2^* in Eq. (6).

When the breakup curves are extensional-like and do not exhibit vertical asymptotes, the same fitting procedure was performed directly on the two parameters K_1 and K_2 without additional modifications. The resulting fits are shown on the right of Fig. 8 and the numerical values are reported in Table 1.

The breakup curves obtained from the fitting procedure and with $f_{2,\mathrm{mod}}$ used in Eq. (19) are shown in Fig. 9. The agreement between the proposed model, the original (circles) and augmented (open squares) experimental data, and the numerical simulations (stars) is very satisfactory. According to the DNS results, a vertical asymptote exists for $\alpha = 0.55$ (at $\lambda \sim 130$) whereas the experiments show an extensional-like behavior for $\alpha \geq 0.6$. Hence, the transition between these two trends is for $0.55 < \alpha < 0.6$ (light blue zone in Fig. 8). The exact value could be obtained by running further DNS simulations for very high viscosity ratios. However, in practical applications the viscosity ratio is generally lower than 100 and, in this range, the breakup curves at $\alpha = 0.55$ and $\alpha = 0.6$ are very close to each other. As a consequence, even within the remaining transition interval, the variation of the predicted critical capillary number is small. From a practical standpoint, $\mathrm{Ca}_{\mathrm{cr}}$ for intermediate values of α can therefore be safely estimated by interpolation between the neighboring calibrated curves. Hence, for values of α lying between the calibrated curves, a linear interpolation in α can be used without introducing significant uncertainty, since the neighboring breakup curves are nearly overlapping in the relevant viscosity-ratio range.

It is worth noting that even for small deviations of α above zero, the curves rapidly collapse onto the extensional-flow curve, indicating that it is sufficient for the strain magnitude to slightly exceed that of the vorticity to strongly enhance the breakup forces.

One limit of the breakup curves derived from the model is at low values of the viscosity ratio where the droplet undergoes extremely large deformations. This results in an increase in the critical $\mathrm{Ca}_{\mathrm{cr}}$ as λ decreases, which cannot be captured by the model. The breakup curves in Fig. 9, indeed, reach a plateau for $\lambda \leq 0.5$.

To accurately describe breakup for $\lambda \leq 0.5$, however, the present framework could be coupled with one of the high-deformation theories for slender bodies available in the literature [37,57–59]. Such an extension would enable the proposed approach to capture breakup also in the low-viscosity-ratio regime, where the dispersed phase is less viscous than the continuous phase and undergoes substantial elongation. Under these conditions, the assumption of an ellipsoidal droplet is no longer valid, making ellipsoidal models inadequate for describing the breakup process.

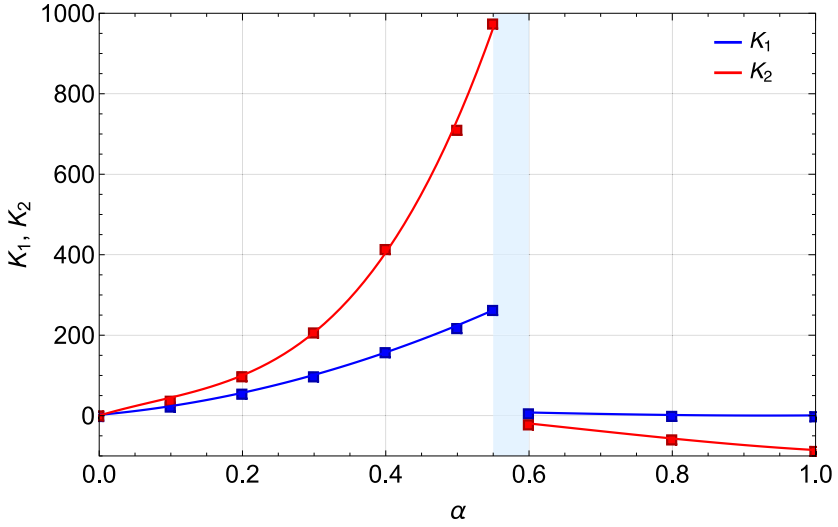

Fig. 8. Fitting results for K_1 and K_2 as a function of α. The light blue shaded region corresponds to a range that was not explored in this study. The blue and red curves on the left-hand side are the following empirical second- and third-degree polynomial fits, respectively, used only to represent the data trend and not endowed with physical meaning: $K_1(\alpha) = 2.15 + 160.2\alpha + 568.9\alpha^2$ and $K_2(\alpha) = 0.38 + 528.5\alpha - 1497.9\alpha^2 + 6766.8\alpha^3$. The right-hand-side curves are quadratic fits of the three available data points. Since only three points are available, the fits should be regarded as guides to the eye rather than as definitive functional forms. The quadratic functions are: $K_1(\alpha) = 63.8 - 131.7\alpha + 68.7\alpha^2$ and $K_2(\alpha) = 145.1 - 339.3\alpha + 108.7\alpha^2$.

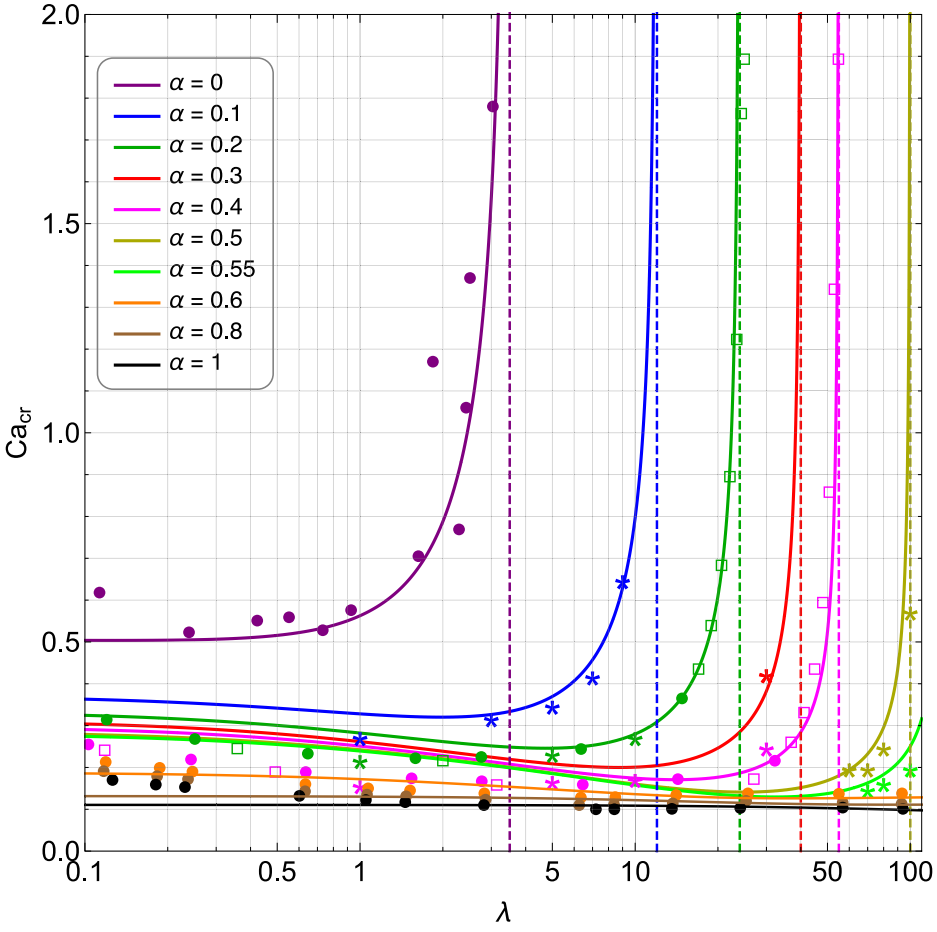

Fig. 9. Breakup curves obtained from the MM model (solid lines) compared with the original (circles) and augmented (open squares) experimental data by Bentley and Leal [37] and Grace [19] and with our direct numerical simulation results (stars) for several hyperbolic flows. The vertical dashed lines are the asymptotes as reported in Grace [19] (for $\alpha = 0$), in Bentley and Leal [37] (for $\alpha = 0.2$ and $\alpha = 0.4$), and computed from our numerical simulations (for $\alpha = 0.1$, $\alpha = 0.3$, $\alpha = 0.5$, and $\alpha = 0.55$).

Table 1
Estimated values of K_1 and K_2, together with their corresponding standard errors. Note that standard errors are not reported for K_2 when $\alpha \leq 0.55$, because these values are not estimated but derived from the asymptotes, as discussed in the text.

α	0	0.1	0.2	0.3	0.4	0.5	0.55	0.6	0.8	1
K_1	1.5	25.2	57.1	100.9	159.8	220.8	265.3	9.5	2.4	0.8
K_2	3.0	39.5	100.2	209.1	416.3	712.7	976.7	−19.3	−56.7	−85.4
SE_{K_1}	0.05	2.4	3.02	5.3	8.1	11.7	17.7	2.96	0.4	0.02
SE_{K_2}	-	-	-	-	-	-	-	1.1	2.2	3.6

An open question is whether breakup of the dispersed phase is possible in flows characterized by a strong vortical component (i.e., for $\alpha \leq 0$). To the best of our knowledge, the literature does not report experimental data showing droplet breakup in elliptic flows. However, a numerical study suggests that for $\alpha \leq -0.3$ the dispersed phase can no longer undergo breakup [45]. To further investigate this point, we performed direct numerical simulations for elliptic flows as well. Our simulations indicate that, once the parameter α becomes negative, the dispersed phase does not undergo breakup for any value of the viscosity ratio. This can be explained by the fact that the trajectories associated with elliptic flows are closed (see Fig. 1), so the droplet never accumulates sufficient strain for breakup to occur. Indeed, the vortical component protects the droplet from large deformations by repeatedly moving it away from the principal stretching direction. This effect is particularly pronounced in elliptic flows, where no unique principal direction exists. Overall, the considerations discussed above for elliptic flows support the conclusion that, under the examined elliptic-flow conditions and assumptions, breakup was not observed. Nevertheless, it is conceivable that breakup of the dispersed phase could still occur in flows where the vortical component exceeds the shear contribution when additional physical effects, such as inertial, gravitational, or confinement effects acting on the dispersed phase are included in the model, aspects that are not considered in the present study. Some indications in this direction and, in general, related to the stability of rotating liquid drops can be found in previous works [60–62].

We emphasize that Eq. (19) requires the existence condition for the critical capillary number, namely $f_2 > |(\alpha - 1)/(\alpha + 1)|$. As it has been shown before, this constraint does not pose any difficulty in deriving breakup curves for hyperbolic flows. In contrast, its treatment may become nontrivial in the case of elliptic flows. Therefore, this existence condition could, in principle, provide theoretical insight into the ranges of α and λ for which the breakup criterion admits a solution. In the present work, however, we do not pursue this approach further, as its conclusions would be strongly dependent on the specific functional form assumed for $f_{2,\mathrm{mod}}$ (that is also α-dependent), thereby limiting the generality and the feasibility of the analysis.

In conclusion to this section, we mention that, if the modified form $f_{2,\mathrm{mod}}$ in Eq. (20) is also used to describe the Taylor deformation parameter D in Eq. (14), the resulting predictions are less accurate than those obtained using the simpler f_2 function for moderate/large Ca. This occurs because the fitting parameters K_1 and K_2 have been calibrated on the breakup data only and not on the entire behavior of D with Ca, implying that the functional form in Eq. (20) is unable to predict both trends. Indeed, the two problems (deformation and breakup) involve different physical ranges of droplet dynamics. The deformation parameter is mainly governed by small-to-moderate deformations, where the ellipsoidal assumption underlying the MM model remains appropriate. Breakup, instead, occurs at large deformations, where the droplet shape departs significantly from an ellipsoid and additional mechanisms such as filament stretching and rupture become relevant. A correction calibrated only on breakup thresholds is therefore not expected to preserve the accuracy of the deformation curve over the whole range of capillary numbers.

A fully unified model would likely require a more complex functional form of f_2 while also satisfying the correct limiting behavior at small deformation, shear flow, and planar extension. Developing such a model would require fitting both deformation and breakup data simultaneously and is beyond the scope of the present work. The present contribution should instead be regarded as a breakup-specific semi-empirical extension of the MM framework aimed at constructing generalized critical capillary numbers for mixed planar flows.

5. Case study: Morphology evolution in a twin-screw extruder

The morphology evolution of mono- and polydisperse blends in a twin-screw extruder has been recently studied by coupling the fluid dynamics within the device to constitutive models that describe the mechanisms undergone by the dispersed phase from the initial to the final state as a function of the applied flow field [32,46,56,63]. A crucial parameter in the procedure to evaluate the blend morphology is the critical capillary number for breakup [64]. As previously mentioned, the effective critical capillary number for $\alpha > 0$ is estimated by assuming a linear interpolation between the shear and extensional critical capillary numbers. This procedure has two issues. First, there is no evidence that the relationship $\mathrm{Ca}_{\mathrm{cr}}(\alpha)$ is linear. Second and more importantly, this procedure cannot be applied for $\lambda > 3.5$ corresponding to the vertical asymptote in shear flow.

In this section, we use the breakup curves obtained in the previous section to predict the morphology of a polymer blend in a 2D twin-screw extruder. As previously done [32,46], the breakup criterion is used here in a quasi-steady sense. Specifically, breakup is assumed to occur whenever the instantaneous local capillary number exceeds the steady-state critical value $\mathrm{Ca}_{\mathrm{cr}}(\alpha, \lambda)$ obtained from the generalized breakup curves. This approximation neglects finite breakup times and the deformation history of the droplet. It is expected to be appropriate when the local flow varies slowly compared with the capillary time scale, or when the droplet remains in a supercritical region for a time sufficiently long for breakup to develop. It is also more reliable when Ca is significantly larger than $\mathrm{Ca}_{\mathrm{cr}}$, since breakup is then expected to occur rapidly. Conversely, close to the critical condition, or when the droplet experiences short intermittent excursions into supercritical regions, the quasi-steady criterion may overestimate breakup because the droplet may leave the region before reaching the deformation required for rupture.

We also note that, in the extruder application, the flow is spatially non-homogeneous and the local flow-type parameter computed as in Eq. (10) is not objective, since it involves the vorticity tensor [55,65]. To overcome this limitation, several objective kinematic descriptors have been proposed in the literature [66–71]. In particular, the theory of (non)-persistence of straining has largely addressed the shortcomings associated with vorticity-based descriptions, providing a robust and reliable framework for characterizing the local flow topology. The impact of using the flow index in Eq. (10) was assessed in our previous work [46] by comparing the Astarita-type index with objective flow-classification criteria, including the corrected Astarita index and the non-persistence-of-straining parameter [68]. The comparison showed that the main differences induced by the non-objective index occur in the classification of shear- and rotation-dominated regions, whereas the identification of extensional versus shear-dominated regions is largely consistent with the objective criteria. Since droplet breakup is mainly controlled by sufficiently extensional flow regions, the qualitative conclusions drawn from the present comparison are not expected to be critically affected by the use of this local index. Nevertheless, the development and implementation of fully objective local breakup criteria

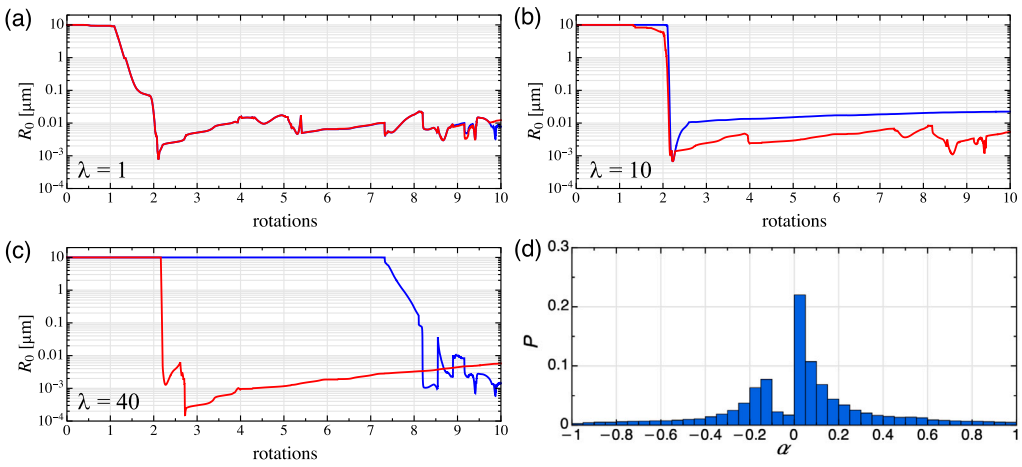

Fig. 10. (a–c) Evolution of the unstretched droplet radius for three viscosity ratios. The blue lines are obtained from the generalized breakup curves. The red curves are obtained with Ca_{cr} either from the linear interpolation between the shear- and extensional-flow values (a), or from assigning the extensional-flow value (b–c). (d) Distribution of the flow index parameter experienced by 100 tracers over 10 screw rotations.

in complex non-homogeneous flows remain an important direction for future work.

We first examine the case at $\lambda = 1$ to highlight the differences between our approach and the commonly used linear interpolation procedure. We then consider $\lambda = 10$ and $\lambda = 40$, both exceeding the viscosity ratio at which the shear flow breakup curve exhibits a vertical asymptote, rendering linear interpolation inapplicable. For these viscosity ratios, we compare the predictions from our generalized breakup curves with those obtained by assuming the critical capillary number to be equal to the extensional-flow value. Although this represents a strong simplification, it is partially supported by experimental evidence indicating that, at high viscosity ratios, the mean size of the dispersed phase is primarily governed by the extensional flow component established within the extruder [72–74]. Accordingly, the Grace curve in pure extensional flow may be adopted as a practical reference to obtain a useful, albeit approximate, estimate for comparative purposes.

We emphasize that the aim of this section is not to introduce a new morphology-evolution model for twin-screw extrusion. The geometrical configuration, the pseudo-homogeneous Newtonian treatment, the Lagrangian tracer methodology, the stretching/unstretched-radius formalism, and the statistical post-processing follow the framework developed by Wong et al. [32,56,63] and, as validation case, in Giglio et al. [46]. The new ingredient introduced here is solely the breakup criterion, namely the replacement of the commonly used linear interpolation between shear and extensional critical capillary numbers, or the extensional-flow approximation at high viscosity ratios, by the generalized breakup curves derived in the previous section. Therefore, the results reported below should be interpreted as a sensitivity study aimed at isolating the effect of the breakup criterion on morphology predictions within an otherwise unchanged computational framework.

The problem consists in a 2D approximation of a fully-intermeshing co-rotating twin-screw extruder. The blend is treated as a pseudo-homogeneous Newtonian fluid. The rotation rate is set to 60 rpm with a total of 10 rotations considered. The morphology evolution is determined by tracking 100 tracers randomly initialized within the domain. We refer to Giglio et al. [46] for the other geometrical, flow, and morphological parameters as well as for the numerical procedure.

Figs. 10a–10c show the evolution of the droplet radius along one typical trajectory of the extruder for the three viscosity ratios. The blue lines are obtained from our generalized breakup curves whereas the red ones are obtained by evaluating Ca_{cr} from the linear interpolation estimate (for $\lambda = 1$) or by assuming it equal to the value in extensional flow (for $\lambda = 10$ and $\lambda = 40$). It can be readily observed that, for the lowest viscosity ratio, the two predictions essentially coincide. Indeed, the difference between the generalized breakup curve and the linear interpolation approximation lies in how the critical capillary number varies between $\alpha = 0$ and $\alpha = 1$. With the generalized curve, the critical capillary number decreases more rapidly than a linear trend, meaning that the linear interpolation systematically overestimates Ca_{cr}. Nevertheless, the deviation between the two predictions remains relatively limited. Since the capillary numbers typically experienced by droplets in a twin-screw extruder are very high (well above the values predicted by either approach) the breakup dynamics remain essentially the same in both cases.

In contrast, pronounced deviations emerge at $\lambda = 10$ as shown in Fig. 10b. The key distinction between the blue and red curves is that the generalized breakup curves have a lower bound of α below which breakup cannot occur, whereas the red curves assume extensional-like behavior for any α, implying that breakup is always possible. As a result, the droplet radius predicted by the generalized breakup curves is larger, since breakup is effectively more difficult to achieve. This difference becomes even more pronounced at $\lambda = 40$ (Fig. 10c), where Fig. 9 shows that no breakup occurs for $\alpha < 0.3$. Indeed, the distribution of the flow type parameter reported in Fig. 10d, computed from 100 tracers over 10 rotations, reveals that the most probable values of α lie between 0 and 0.2. Consequently, for most of its residence time, the droplet does not undergo breakup unless it reaches regions characterized by sufficiently high α.

These trends are reflected in the droplet radius distributions shown in Figs. 11, 12, and 13 for $\lambda = 1$, 10, and 40. For $\lambda = 1$, only minor differences appear between the left panels (generalized breakup curves) and the right panels (linear interpolation). In contrast, quantitative discrepancies become evident at $\lambda = 10$ and are even more pronounced at $\lambda = 40$. In this latter case, the final particle size distribution after 10 rotations is bimodal with a fraction of droplets that did not breakup, reflecting the fact that breakup becomes more difficult than predicted by the extensional-like critical capillary number. Indeed, the generalized breakup criterion predicts that breakup is possible only when droplets experience sufficiently extension-dominated regions. As a result, at finite residence times two droplet families may coexist: droplets that encounter high-α regions and undergo breakup, and droplets that remain mainly in shear-like or weakly deforming regions, where breakup is inhibited. This mechanism is consistent with previous numerical studies of morphology evolution in complex flows, where different trajectory classes were shown to produce distinct breakup histories [32,46]. At high viscosity ratio, this trajectory-dependent behavior becomes more pronounced and can lead to the bimodal particle-size distributions observed in the present simulations. Further experimental or direct numerical evidence at high viscosity ratios would be valuable to quantitatively validate this prediction.

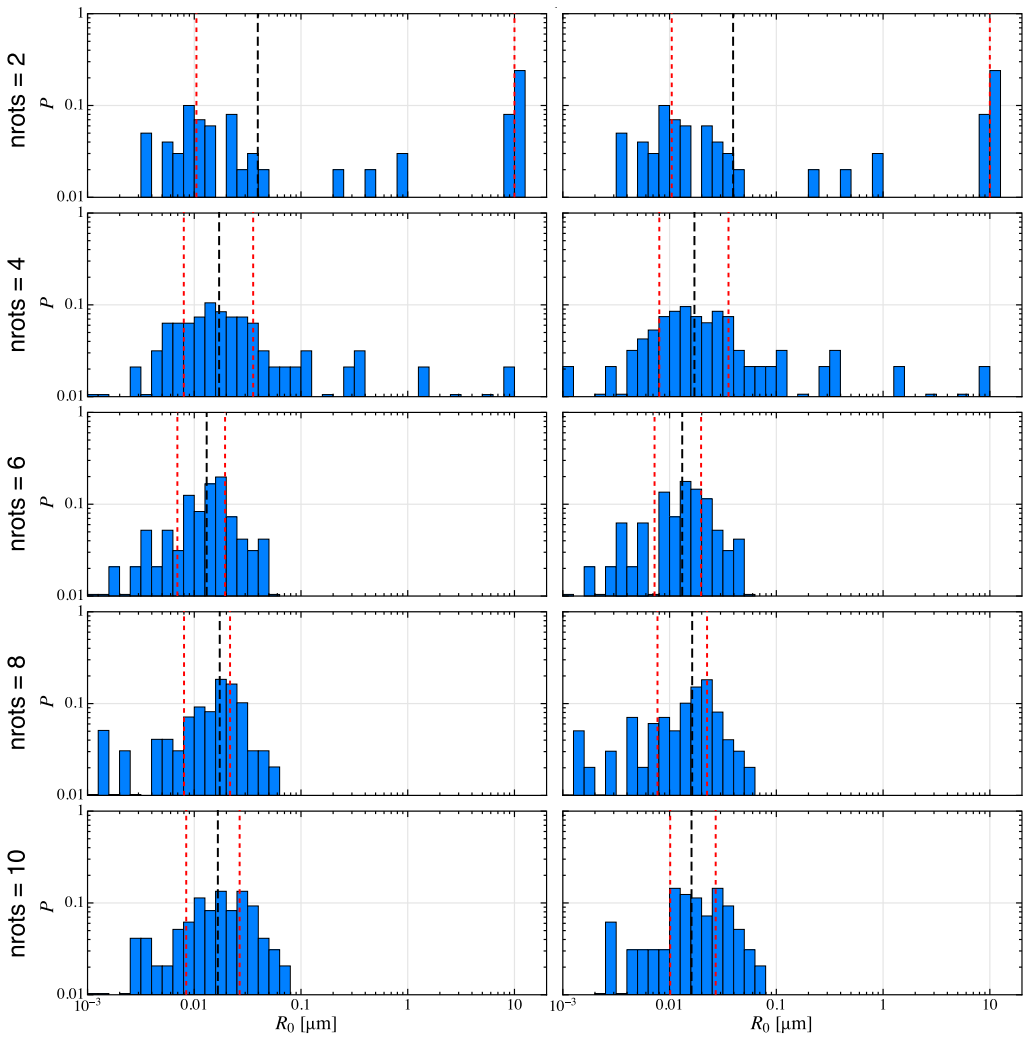

Fig. 11. Unstretched droplet radius distributions at different rotations obtained from the generalized breakup curves (left) and from the linear interpolation estimate (right). The viscosity ratio is $\lambda = 1$. The black dashed line is the median value, whereas the two red dashed lines are the first and third quartile.

We also analyzed the case $\lambda = 80$ (not shown), for which no breakup occurs when $\alpha < 0.49$ according to Fig. 9. Since the α-distribution in Fig. 10d indicates that droplets rarely encounter regions with $\alpha > 0.5$, the droplet radius distribution remains essentially unchanged after 10 rotations. In contrast, assuming the critical capillary number to be equal to the extensional value produces an evolution similar to that observed at lower λ.

Naturally, the flow index experienced by a droplet depends on the geometry of the extruder. In the 2D approximation, shear-like regions dominate, leading to smaller effective values of α. In a fully 3D twin-screw extruder, however, breakup is much more likely, as the flow type parameter can readily reach values of 0.8 or higher [46]. Indeed, the three-dimensional helical flow enhances strain in the third direction, thus promoting droplet breakup far more effectively than in 2D configurations.

6. Conclusions and future perspectives

In this work, we solved the steady-state form of the Maffettone–Minale model to derive analytical expressions for the three semiaxes of an ellipsoidal droplet subjected to general planar mixed flows, spanning from pure rotation to shear and planar extension. From these solutions, we obtained general expressions for the Taylor deformation parameter and the droplet orientation angle as a function of the flow parameter and the viscosity ratio. The model predictions agree very well with experimental and numerical simulation results for both hyperbolic and elliptic flows, provided that the capillary number is not too large.

Using this framework, we also derived analytical breakup curves for general two-dimensional flows by keeping the same structure of the improved function f_2 in the original model and introducing new parameters that vary with the flow type. These parameters have been calibrated with available experimental data and novel direct numerical simulations performed in this study. These curves correctly describe the breakup in hyperbolic flows except at very low values of the viscosity ratio. In such situations, a slender-body model would be required to properly describe the breakup of highly elongated filaments. The direct numerical simulation results suggest that droplet breakup may not occur in elliptic flows under the present assumptions, namely in the absence of inertial, gravitational, and confinement effects acting on the dispersed phase. We stress that the proposed modification of f_2 is specifically calibrated for breakup and does not constitute a unified improvement of the MM model for both deformation and breakup. The original MM formulation remains more appropriate for predicting the Taylor deformation parameter, whereas the modified expression provides a practical semi-empirical route to obtain generalized breakup curves in mixed planar flows.

The generalized breakup curves were also tested within an existing morphology-evolution framework for a two-dimensional twin-screw

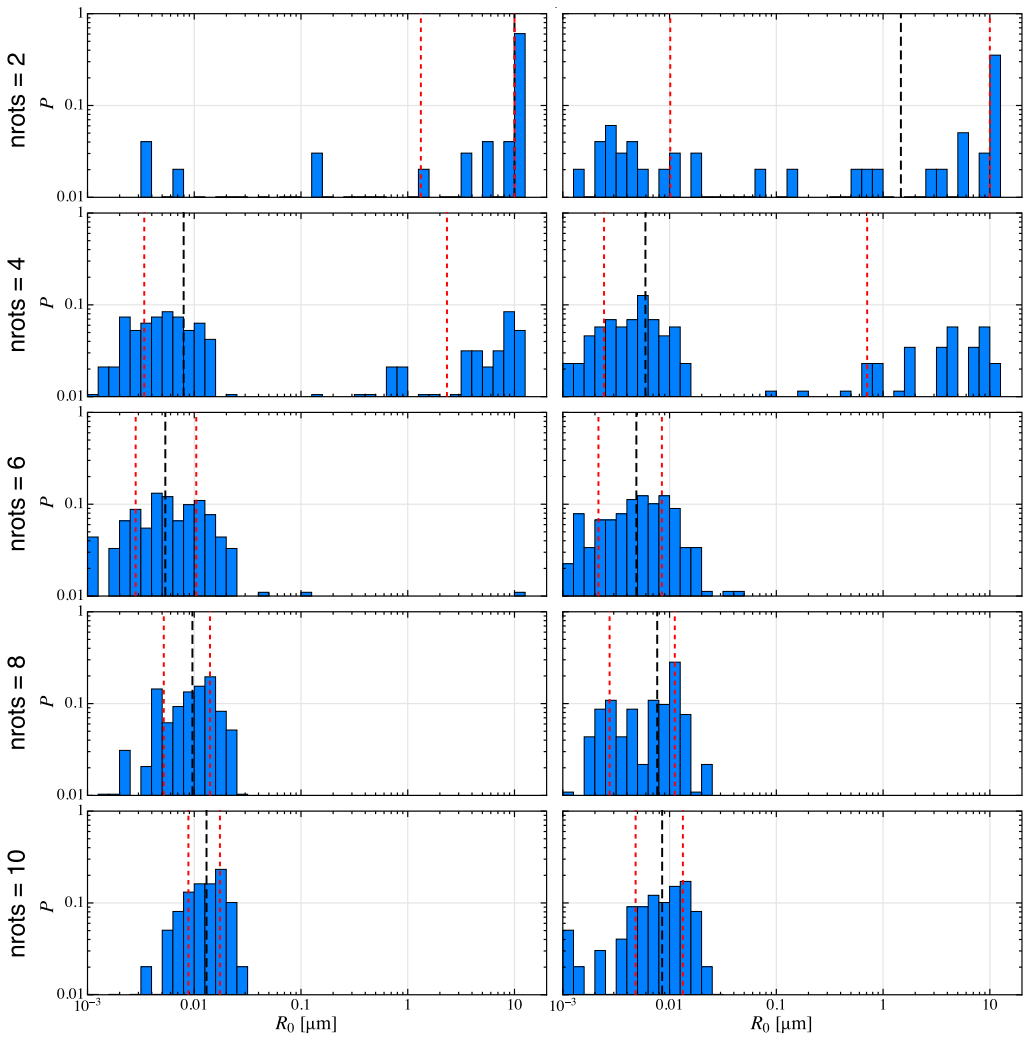

Fig. 12. Unstretched droplet radius distributions at different rotations obtained from the generalized breakup curves (left) and by assuming the critical capillary number equal to the one in extensional flow (right). The viscosity ratio is $\lambda = 10$. The black dashed line is the median value, whereas the two red dashed lines are the first and third quartile.

extruder configuration. This application was intended as an illustrative sensitivity study of the breakup criterion, while all other elements of the morphology model were kept unchanged with respect to previous works. For low viscosity ratios, both the generalized breakup criterion and the standard linear interpolation assumption yield similar predictions, since the capillary numbers typically encountered in the extruder far exceed the corresponding critical values. However, for higher viscosity ratios, significant differences arise. The generalized breakup curves incorporate a lower bound on the flow type parameter, below which breakup cannot occur, whereas extensional-based criteria predict breakup under all conditions. As a consequence, the generalized model yields larger droplet radii and reduced breakup frequency, consistent with the more restrictive breakup conditions. This highlights the risk of overestimating breakup in simulations based on simplified critical capillary number assumptions.

The results presented in this work demonstrate that, within its intended range of validity, our approach offers a robust and efficient tool for predicting droplet deformation, orientation, and breakup in steady complex flows. Therefore, it is well suited for implementation in computational models of mixing processes commonly found in industrial equipment, such as twin-screw extruders, static mixers, and four-roll mills, allowing to improve the prediction of particle size distributions, which critically influence the final material properties.

CRediT authorship contribution statement

Michele Giglio: Writing – review & editing, Writing – original draft, Software, Methodology, Investigation, Data curation, Conceptualization. **Giancarlo Esposito:** Writing – review & editing, Writing – original draft, Validation, Software, Methodology, Investigation, Formal analysis, Data curation. **Gaetano D'Avino:** Writing – review & editing, Writing – original draft, Validation, Supervision, Software, Methodology, Investigation, Formal analysis, Conceptualization. **Massimiliano Maria Villone:** Writing – review & editing, Writing – original draft, Validation, Supervision, Software, Methodology, Investigation, Formal analysis, Conceptualization. **Pier Luca Maffettone:** Writing – review & editing, Supervision, Methodology, Funding acquisition, Conceptualization.

Declaration of competing interest

The authors declare that they have no known competing financial interests or personal relationships that could have appeared to influence the work reported in this paper.

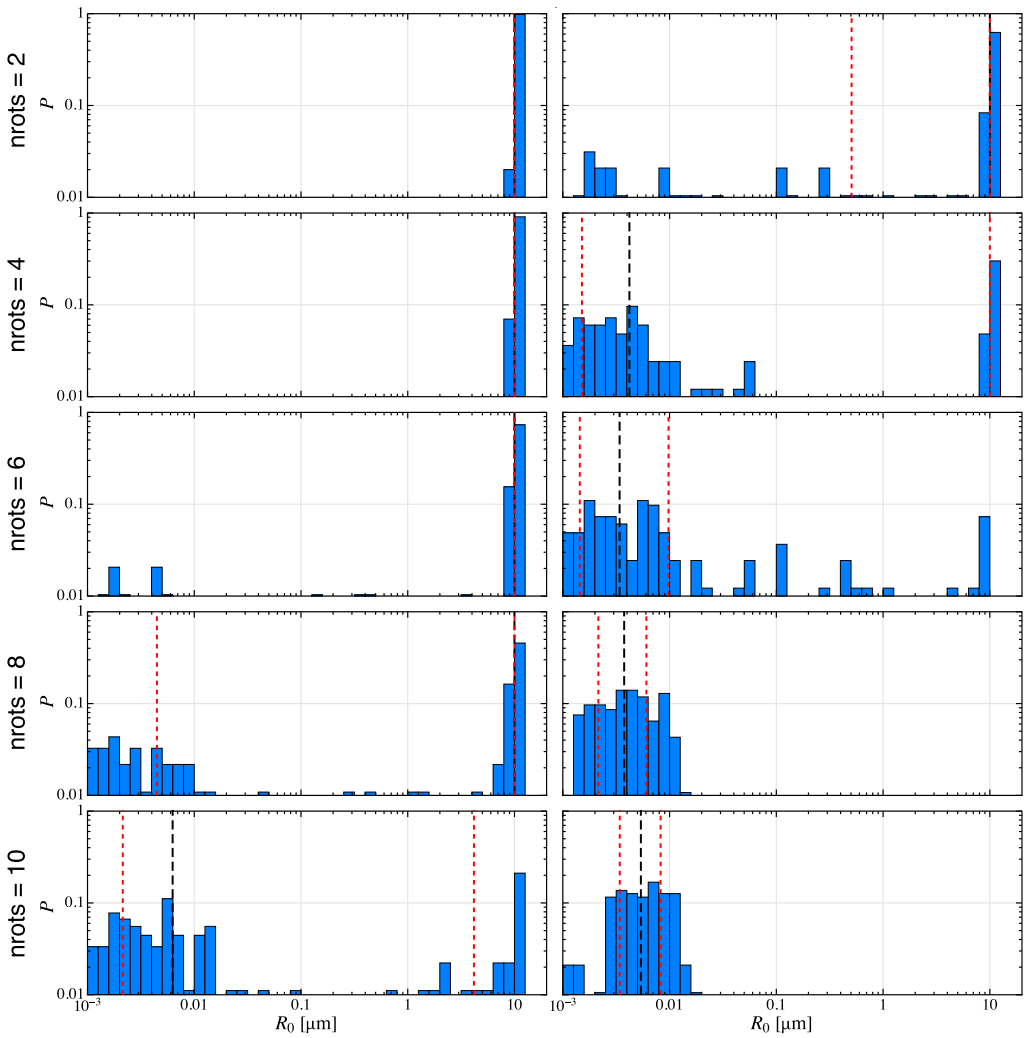

Fig. 13. Unstretched droplet radius distributions at different rotations obtained from the generalized breakup curves (left) and by assuming the critical capillary number equal to the one in extensional flow (right). The viscosity ratio is $\lambda = 40$. The black dashed line is the median value, whereas the two red dashed lines are the first and third quartile.

Acknowledgments

G. D'Avino acknowledges the financial support of the Italian Ministry of University and Research (MUR) under the program "Progetti di Rilevante Interesse Nazionale", Grant 20229WJBPS. The authors also acknowledge the use of the high performance computing cluster IBISCo funded by project PIR01_00011, PON 2014–2020.

Appendix. Numerical formulation and setup

In this appendix, we briefly summarize the problem setup and the methodology employed for the numerical simulations.

The numerical analysis was performed using two distinct approaches: the interface-tracking Arbitrary Lagrangian–Eulerian (ALE) method and the interface-capturing geometric Volume-of-Fluid (VOF) approach. This combined strategy is motivated by the complementary strengths and limitations of the two formulations. The ALE method, being boundary-fitted, explicitly treats the interface as a moving boundary on which interfacial conditions can be directly imposed, resulting in high accuracy [75]. For this reason, it is employed to investigate drop deformation in regimes sufficiently far from breakup. However, its formulation does not naturally accommodate topological changes and, in addition, its performance deteriorates at large deformations due to increasing mesh skewness.

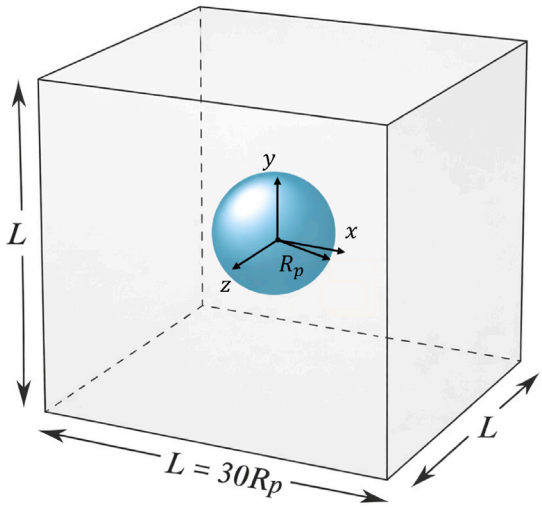

Fig. A.1. Schematic representation of the physical system. An initially spherical drop of radius R_p is suspended in a Newtonian fluid within a cubic computational domain of size $L = 30R_p$. The origin of the Cartesian reference frame is located at the center of the drop.

In contrast, the geometric VOF method provides a conservative interface-capturing framework in which the interface evolution is reconstructed from the advection of a color function representing the phase distribution [76]. This makes it particularly suitable for assessing breakup conditions and handling large interfacial deformations. Preliminary tests have confirmed that, in regimes far from breakup, the two methods yield essentially identical results, thereby ensuring consistency between the approaches.

The system under investigation is shown in Fig. A.1. It consists of a single deformable drop of radius R_p suspended in a surrounding fluid contained within a cubic domain of side length $L = 30R_p$. The domain size is chosen sufficiently large to minimize confinement effects and approximate unbounded flow conditions.

Assuming isothermal conditions, incompressible fluids, and negligible inertia, the governing equations for both phases reduce to the continuity and momentum balance equations:

$$\nabla \cdot \boldsymbol{u} = 0, \tag{A.1}$$

$$\nabla \cdot \boldsymbol{\sigma} = \boldsymbol{0}, \tag{A.2}$$

where $\boldsymbol{u}$ denotes the velocity field and $\boldsymbol{\sigma}$ is the Cauchy stress tensor. The latter is expressed as:

$$\boldsymbol{\sigma} = -p\boldsymbol{I} + \boldsymbol{T}, \tag{A.3}$$

with p the pressure, $\boldsymbol{I}$ the identity tensor, and $\boldsymbol{T}$ the deviatoric stress tensor. For Newtonian fluids, the constitutive equation reads:

$$\boldsymbol{T} = 2\eta\boldsymbol{D}, \tag{A.4}$$

where η is the dynamic viscosity, and $\boldsymbol{D}$ is the rate-of-deformation tensor defined as:

$$\boldsymbol{D} = \frac{1}{2}\left(\nabla\boldsymbol{u} + (\nabla\boldsymbol{u})^T\right). \tag{A.5}$$

The boundary conditions imposed on the outer surfaces of the computational domain correspond to a homogeneous linear flow field. Rather than specifying the velocity components on each boundary separately, they can be compactly written as:

$$\boldsymbol{u}(\boldsymbol{x}) = \boldsymbol{\nabla u} \cdot \boldsymbol{x}, \tag{A.6}$$

where $\boldsymbol{\nabla u}$ is the constant velocity gradient tensor (see Eq. (7)). The resulting velocity field is:

$$u_x = G\left[\frac{1}{2}(1+\alpha)x + \frac{1}{2}(1-\alpha)y\right], \tag{A.7}$$

$$u_y = G\left[-\frac{1}{2}(1-\alpha)x - \frac{1}{2}(1+\alpha)y\right], \tag{A.8}$$

$$u_z = 0. \tag{A.9}$$

At the drop–matrix interface, continuity of velocity is enforced together with a balance of stresses. In particular, the jump in the normal stress is balanced by capillary forces:

$$\left(\boldsymbol{\sigma}_m - \boldsymbol{\sigma}_d\right) \cdot \boldsymbol{n} = \sigma\,\boldsymbol{n}\nabla \cdot \boldsymbol{n}, \tag{A.10}$$

where σ is the interfacial tension, $\boldsymbol{n}$ is the unit normal vector pointing outward from the drop and the subscripts ‘m’ and ‘d’ refer to the matrix and drop phases.

Interface tracking simulations

For the interface-tracking simulations, the governing equations are solved using an arbitrary Lagrangian–Eulerian (ALE) finite element formulation, which enables explicit tracking of the interface motion. The normal velocity of the interface is set equal to the normal component of the fluid velocity, while the tangential velocity is defined to maintain a high-quality mesh distribution along the interface.

This approach prevents excessive mesh distortion associated with the tank-treading motion of the drop and significantly improves numerical stability compared to a purely Lagrangian formulation. Both the drop and matrix domains are discretized using quadratic tetrahedral elements, while the interface is represented by conforming quadratic triangular elements, ensuring geometric continuity across phases.

Spatial and temporal convergence tests are performed for all the investigated cases. The mesh resolution and time step are selected such that further refinements do not affect the results. Typically, meshes comprising 2×10^4–4×10^4 tetrahedral elements and time steps of order $10^{-3}\,G^{-1}$ are found to provide grid and time independent solutions. Further details concerning the numerical schemes can be found in Ref. [75].

Interface capturing simulations

The interface-capturing numerical simulations are performed using the open-source finite-volume solver Basilisk [76]. This solver has been extensively validated for free-surface flows and multiphase systems [77].

The governing equations are solved on a Cartesian grid using a collocated arrangement for the velocity and pressure. The interface between the two phases is captured using a geometric Volume-of-Fluid (VOF) approach, based on the advection of an indicator function ϕ. This approach relies on a one-fluid formulation, in which the local density and viscosity are defined as weighted averages of the corresponding properties of the two phases. The weighting factor is the indicator function ϕ, which represents the volumetric fraction of one of the two phases within each computational cell. The value of ϕ is bounded between 0 and 1. It is $\phi = 1$ when the computational cell is entirely occupied by the suspended drop, $\phi = 0$ when it is fully occupied by the surrounding matrix, and $0 < \phi < 1$ in interfacial cells containing both phases.

The evolution of the interface is governed by the advection of indicator function:

$$\frac{\partial\phi}{\partial t} + \boldsymbol{u} \cdot \nabla\phi = 0. \tag{A.11}$$

The density and viscosity fields are computed as weighted averages of the properties of the two phases, according to

$$\rho(\phi) = \phi\,\rho_d + (1-\phi)\rho_m, \tag{A.12}$$

$$\eta(\phi) = \phi\,\eta_d + (1-\phi)\eta_m. \tag{A.13}$$

To accurately resolve the interface and the complex flow features, an adaptive mesh refinement (AMR) strategy based on wavelet decomposition is employed [78]. The mesh is dynamically refined according to the estimated error on the velocity field, the curvature and the indicator function ϕ. This choice ensures that the highest resolution is achieved in the regions of interest, namely near the drop interface. The refinement procedure is controlled by three parameters: the initial refinement level N, the maximum level N_{max}, and the minimum level N_{min}. These parameters define the local grid size Δx according to

$$\Delta x = \frac{L}{2^N}, \tag{A.14}$$

where L is the domain size. To minimize errors in the initial representation of the drop volume, the entire computational domain is initially refined uniformly. As the simulation progresses and the drop deforms, the mesh is dynamically adapted according to the refinement criteria described above.

The time integration is performed using a second-order fractional-step method [79]. The time step Δt is restricted by the capillary time scale to limit the occurrence of spurious capillary waves [76], such that $\Delta t \le \Delta t_\sigma$ where Δt_σ is the capillary time-step constraint.

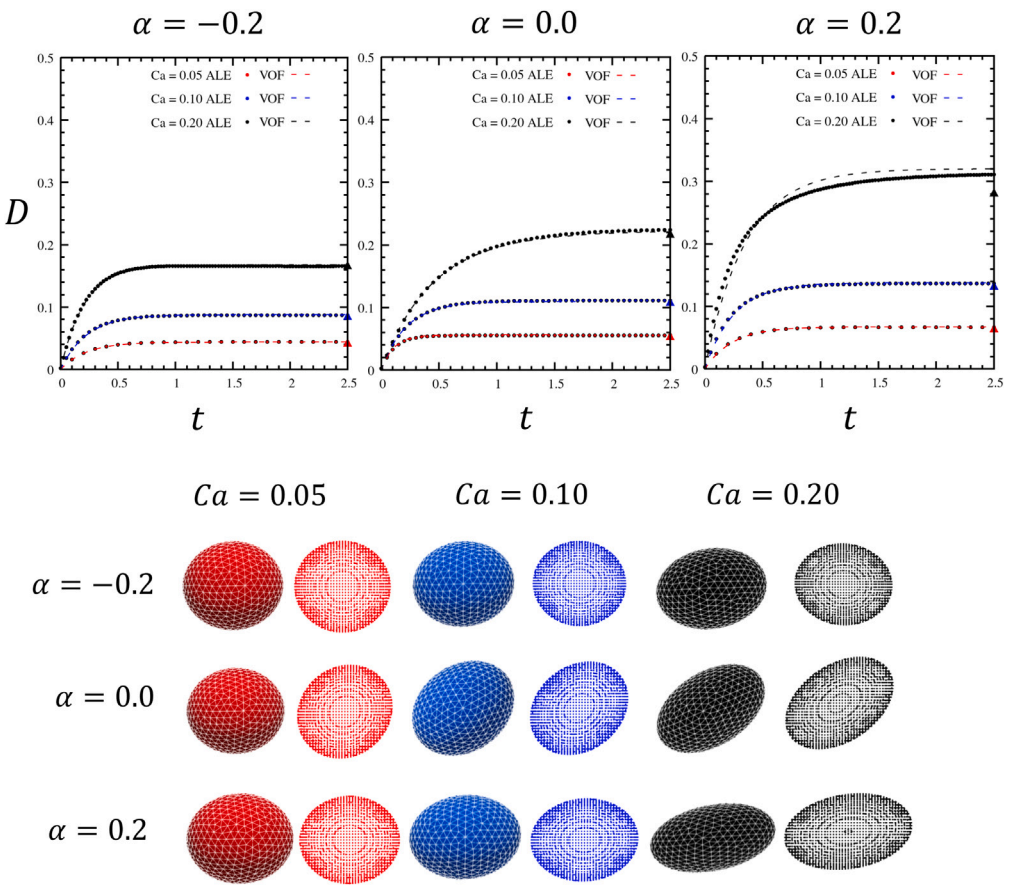

Fig. A.2. Upper row: Time evolution of the Taylor deformation parameter, D, for three capillary numbers, Ca, under different flow types: elliptic ($\alpha = -0.2$), simple shear ($\alpha = 0$), and hyperbolic ($\alpha = 0.2$), at $\lambda = 1$. Circles represent DNS results obtained with the interface-tracking ALE method, while dashed lines correspond to predictions from the interface-capturing VOF method. Symbols indicate the MM model predictions. Bottom row: Comparison of the steady-state droplet shapes. Results obtained with the interface-tracking ALE method are shown in the first, third, and fifth columns, while those obtained with the interface-capturing VOF method are shown in the second, fourth, and sixth columns.

Validation of the numerical setup: ALE vs VOF

To assess the accuracy of the numerical implementation, Fig. A.2 compares the interface-tracking ALE method with the interface-capturing VOF method in terms of the temporal evolution of the Taylor deformation parameter, D. Results are presented for three capillary numbers, Ca, under different flow kinematics, namely elliptic flow ($\alpha = -0.2$), simple shear flow ($\alpha = 0$), and hyperbolic flow ($\alpha = 0.2$), all at viscosity ratio $\lambda = 1$.

Overall, very good agreement is observed between the ALE and VOF approaches across all cases, demonstrating the consistency of the two numerical frameworks. Furthermore, both methods show excellent agreement with the MM model predictions in the small-deformation regime. As the deformation increases, however, the MM model slightly underpredicts the steady-state value of D, with deviations becoming more noticeable at higher capillary numbers. The droplet shapes shown in the figure further confirm the consistency between the two numerical approaches across the different flow types.

Data availability

Data will be made available on request.

References

[1] C.D. Han, Multiphase flow in polymer processing, in: Rheology: Volume 3: Applications, Springer, 1981, pp. 121–128.
[2] K. Kar, R. Cope, J. Lueske, Mixing Process Technology: A Guide to Industrial Applications, CRC Press, 2025.
[3] L.A. Utracki, C.A. Wilkie, Polymer Blends Handbook, Springer Dordrecht, 2014.
[4] R.P. Chhabra, S.A. Patel, Bubbles, Drops, and Particles in Non-Newtonian Fluids, CRC Press, 2023.
[5] J.K. Lee, C.D. Han, Evolution of polymer blend morphology during compounding in a twin-screw extruder, Polymer 41 (2000) 1799–1815, http://dx.doi.org/10.1016/s0032-3861(99)00325-0.
[6] H.E.H. Meijer, J.M.H. Janssen, P.D. Anderson, Mixing and Compounding of Polymers: Theory and Practice, Hanser, New York, 1994, pp. 85–148.
[7] L. Erwin, Principles of Laminar Fluid/fluid Mixing, Marcel Dekker New York, 1991.
[8] I.M. Zloczower, Z. Tadmor, Mixing and Compounding of Polymers: Theory and Practice, Hanser, New York, 1994.
[9] J.M.H. Janssen, H.E.H. Meijer, Dynamics of liquid-liquid mixing: A 2-zone model, Polym. Eng. Sci. 35 (1995) 1766–1780, http://dx.doi.org/10.1002/pen.760352206.
[10] J.M. Rallison, The deformation of small viscous drops and bubbles in shear flows, Annu. Rev. Fluid Mech. 16 (1984) 45–66, http://dx.doi.org/10.1146/annurev.fl.16.010184.000401.
[11] G.I. Taylor, The viscosity of a fluid containing small drop ofanother fluid, Proc. R. Soc. Lond. A. 138 (1932) 41–48, http://dx.doi.org/10.1098/rspa.1932.0169.
[12] G.I. Taylor, The formation of emulsion in definable field offlow, Proc. R. Soc. Lond. A. 146 (1934) 501–523, http://dx.doi.org/10.1098/rspa.1934.0169.
[13] H.A. Stone, Dynamics of drop deformation and breakup in viscous fluids, Annu. Rev. Fluid Mech. 26 (1994) 65–102, http://dx.doi.org/10.1146/annurev.fl.26.010194.000433.
[14] F. Greco, Drop deformation for non-Newtonian fluids in slow flows, J. Non-Newton. Fluid Mech. 107 (2002) 111–131, http://dx.doi.org/10.1016/S0377-0257(02)00144-1.
[15] S. Guido, F. Greco, et al., Dynamics of a liquid drop in a flowing immiscible liquid, in: Rheology Reviews, Cambrian Printers and the British Society of Rheology, 2004, pp. 99–142.

[16] V. Cristini, Y.-C. Tan, Theory and numerical simulation of droplet dynamics in complex flows—a review, Lab Chip 4 (2004) 257–264, http://dx.doi.org/10.1039/B403226H.

[17] M. Minale, Models for the deformation of a single ellipsoidal drop: a review, Rheol. Acta 49 (2010) 789–806, http://dx.doi.org/10.1007/s00397-010-0442-0.

[18] I. Fortelnỳ, J. Juza, Description of the droplet size evolution in flowing immiscible polymer blends, Polymers 11 (2019) 761, http://dx.doi.org/10.3390/polym11050761.

[19] H.P. Grace, Dispersion phenomena in high viscosity immiscible fluid systems and application of static mixers as dispersion devices in such systems, Chem. Eng. Commun. 14 (1982) 225–277, http://dx.doi.org/10.1080/00986448208911047.

[20] P.L. Maffettone, M. Minale, Equation of change for ellipsoidal drops in viscous flow, J. Non-Newton. Fluid Mech. 78 (1998) 227–241, http://dx.doi.org/10.1016/s0377-0257(98)00065-2.

[21] P.L. Maffettone, F. Greco, Ellipsoidal drop model for single drop dynamics with non-Newtonian fluids, J. Rheol. 48 (2004) 83–100, http://dx.doi.org/10.1122/1.1626675.

[22] M. Minale, Deformation of a non-Newtonian ellipsoidal drop in a non-Newtonian matrix: extension of Maffettone–Minale model, J. Non-Newton. Fluid Mech. 123 (2004) 151–160, http://dx.doi.org/10.1016/j.jnnfm.2004.07.017.

[23] N.E. Jackson, C.L. Tucker, A model for large deformation of an ellipsoidal droplet with interfacial tension, J. Rheol. 47 (2003) 659–682, http://dx.doi.org/10.1122/1.1562152.

[24] V.T. Hoang, J.M. Park, A taylor analogy model for droplet dynamics in planar extensional flow, Chem. Eng. Sci. 204 (2019) 27–34, http://dx.doi.org/10.1016/j.ces.2019.04.015.

[25] V. Thanh Hoang, H.-T. Do-Le, D. Hung Vo, Improved Taylor analogy model for predicting droplet breakup and large deformation in planar extensional flow, Chem. Eng. Sci. 282 (2023) 119232, http://dx.doi.org/10.1016/j.ces.2023.119232.

[26] T.T. Nguyen, V.T. Hoang, Modeling droplet deformation and breakup in shear flow using taylor analogy model, Chem. Eng. Sci. 320 (2026) 122370, http://dx.doi.org/10.1016/j.ces.2025.122370.

[27] J.M.H. Janssen, H.E.H. Meijer, Droplet breakup mechanisms: Stepwise equilibrium versus transient dispersion, J. Rheol. 37 (1993) 597–608, http://dx.doi.org/10.1122/1.550385.

[28] V. Cristini, J. Bławzdziewicz, M. Loewenberg, Drop breakup in three-dimensional viscous flows, Phys. Fluids 10 (1998) 1781–1783, http://dx.doi.org/10.1063/1.869697.

[29] Y.W. Stegeman, F.N. Van De Vosse, H.E.H. Meijer, On the applicability of the grace curve in practical mixing operations, Can. J. Chem. Eng. 80 (2002) 1–6, http://dx.doi.org/10.1002/cjce.5450800414.

[30] H.A. Stone, L.G. Leal, The influence of initial deformation on drop breakup in subcritical time-dependent flows at low Reynolds numbers, J. Fluid Mech. 206 (1989) 223–263, http://dx.doi.org/10.1017/S0022112089002296.

[31] H.A. Stone, L.G. Leal, Relaxation and breakup of an initially extended drop in an otherwise quiescent fluid, J. Fluid Mech. 198 (1989) 399–427, http://dx.doi.org/10.1017/S0022112089000194.

[32] W.-H.B. Wong, V.G. de Bie, M.A. Hulsen, P.D. Anderson, Numerical modeling of the blend morphology evolution in twin-screw extruders, Macromol. Theory Simul. 31 (2022) 2270005, http://dx.doi.org/10.1002/mats.202100087.

[33] P.J.A. Janssen, A. Vananroye, P. Van Puyvelde, P. Moldenaers, P.D. Anderson, Generalized behavior of the breakup of viscous drops in confinements, J. Rheol. 54 (2010) 1047–1060, http://dx.doi.org/10.1122/1.3473924.

[34] H.A. Stone, L.G. Leal, The effects of surfactants on drop deformation and breakup, J. Fluid Mech. 220 (1990) 161–186, http://dx.doi.org/10.1017/S0022112090003226.

[35] I.B. Bazhlekov, P.D. Anderson, H.E.H. Meijer, Numerical investigation of the effect of insoluble surfactants on drop deformation and breakup in simple shear flow, J. Colloid Interface Sci. 298 (2006) 369–394, http://dx.doi.org/10.1016/j.jcis.2005.12.017.

[36] B.J. Bentley, L.G. Leal, A computer-controlled four-roll mill for investigations of particle and drop dynamics in two-dimensional linear shear flows, J. Fluid Mech. 167 (1986) 219, http://dx.doi.org/10.1017/s002211208600280x.

[37] B.J. Bentley, L.G. Leal, An experimental investigation of drop deformation and breakup in steady, two-dimensional linear flows, J. Fluid Mech. 167 (1986) 241, http://dx.doi.org/10.1017/s0022112086002811.

[38] I.Y. Rosas, M.A.H. Reyes, A.A. Minzoni, E. Geffroy, Computer-controlled two-roll mill flow cell for the experimental study of particle and drop dynamics, Exp. Therm. Fluid Sci. 60 (2015) 54–65, http://dx.doi.org/10.1016/j.expthermflusci.2014.08.006.

[39] E. Boonen, P. Van Puyvelde, P. Moldenaers, Droplet dynamics in sub-critical complex flows, Rheol. Acta 48 (2009) 359–371, http://dx.doi.org/10.1007/S00397-008-0322-Z.

[40] E. Boonen, P.V. Puyvelde, P. Moldenaers, Single droplet break-up in controlled mixed flows, ACS Appl. Mater. Interfaces 2 (2010) 2140–2146, http://dx.doi.org/10.1021/am100389x.

[41] K. Feigl, S.F.M. Kaufmann, P. Fischer, E.J. Windhab, A numerical procedure for calculating droplet deformation in dispersing flows and experimental verification, Chem. Eng. Sci. 58 (2003) 2351–2363, http://dx.doi.org/10.1016/S0009-2509(03)00078-2.

[42] D.I. Bigio, C.R. Marks, R.V. Calabrese, Predicting drop breakup in complex flows from model flow experiments, Int. Polym. Process. 13 (1998) 192–198, http://dx.doi.org/10.3139/217.980192.

[43] F.D. Godbille, J.J.C. Picot, Drop breakup in combined shear and extensional flow conditions, Adv. Polym. Technol. 19 (2000) 14–21, http://dx.doi.org/10.1002/(SICI)1098-2329(20000117)19:1<14::AID-ADV2>3.0.CO;2-F.

[44] J.M. Rallison, Note on the time-dependent deformation of a viscous drop which is almost spherical, J. Fluid Mech. 98 (1980) 625–633, http://dx.doi.org/10.1017/s0022112080000316.

[45] J.M. Rallison, A numerical study of the deformation and burst of a viscous drop in general shear flows, J. Fluid Mech. 109 (1981) 465–482, http://dx.doi.org/10.1017/s002211208100116x.

[46] M. Giglio, M. Trofa, G. D'Avino, M.M. Villone, G. Marchetti, A. La Piccirella, P.L. Maffettone, Numerical simulation of the fluid dynamics and morphology of a polymeric blend in a twin-screw extruder, Rheol. Acta 64 (2025) 709—-728, http://dx.doi.org/10.1007/s00397-025-01497-9.

[47] H. Yu, Z. Wang, G. Liu, B. Xu, J. Huang, L. Tan, Breakup of viscoelastic droplets in an asymmetric twin-screw extruder, J. Food Eng. 399 (2025) 112635, http://dx.doi.org/10.1016/j.jfoodeng.2025.112635.

[48] G. Wu, B. Xu, L. Tan, H. Yu, J. Huang, L.-S. Turng, Conveying and breakup of a viscoelastic droplet in a dual-speed co-rotating non-twin screw extruder with multi-perturbation rings, Chem. Eng. Sci. 304 (2025) 121116, http://dx.doi.org/10.1016/j.ces.2024.121116.

[49] H. Yu, P. Dong, B. Xu, W. Xu, J. Huang, L. Tan, Q. Wang, L.-S. Turng, Simulation of flow and mixing of partially-filled fluid in an asymmetric twin-screw extruder with an internal baffle using moving-particle semi-implicit method, Chem. Eng. Sci. 318 (2025) 122198, http://dx.doi.org/10.1016/j.ces.2025.122198.

[50] S. Guido, M. Minale, P.L. Maffettone, Drop shape dynamics under shear-flow reversal, J. Rheol. 44 (2000) 1385–1399, http://dx.doi.org/10.1122/1.1315310.

[51] S. Guido, M. Grosso, P.L. Maffettone, Newtonian drop in a Newtonian matrix subjected to large amplitude oscillatory shear flows, Rheol. Acta 43 (2004) 575–583, http://dx.doi.org/10.1007/s00397-004-0388-1.

[52] L. Biferale, C. Meneveau, R. Verzicco, Deformation statistics of sub-Kolmogorov-scale ellipsoidal neutrally buoyant drops in isotropic turbulence, J. Fluid Mech. 754 (2014) 184–207, http://dx.doi.org/10.1017/jfm.2014.366.

[53] F. Guglietta, D. Taglienti, M. Sbragaglia, Deformation of ellipsoidal droplets in homogeneous and isotropic turbulence, Phys. Rev. Fluids 10 (2025) 093601, http://dx.doi.org/10.1103/zhzf-q2b9.

[54] E. Boonen, P. Van Puyvelde, P. Moldenaers, Droplet dynamics in mixed flow conditions: Effect of shear/elongation balance and viscosity ratio, J. Rheol. 54 (2010) 1285–1306, http://dx.doi.org/10.1122/1.3490661.

[55] R.J. Poole, Inelastic and flow-type parameter models for non-Newtonian fluids, J. Non-Newton. Fluid Mech. 320 (2023) 105106, http://dx.doi.org/10.1016/j.jnnfm.2023.105106.

[56] W.-H.B. Wong, P.J.A. Janssen, M.A. Hulsen, P.D. Anderson, Numerical simulations of the polydisperse droplet size distribution of disperse blends in complex flow, Rheol. Acta 60 (2021) 187–207, http://dx.doi.org/10.1007/s00397-021-01258-4.

[57] E.J. Hinch, A. Acrivos, Steady long slender droplets in two-dimensional straining motion, J. Fluid Mech. 91 (1979) 401–414, http://dx.doi.org/10.1017/S0022112079000227.

[58] E.J. Hinch, A. Acrivos, Long slender drops in a simple shear flow, J. Fluid Mech. 98 (1980) 305–328, http://dx.doi.org/10.1017/S0022112080000171.

[59] D. Khakhar, J. Ottino, Deformation and breakup of slender drops in linear flows, J. Fluid Mech. 166 (1986) 265–285, http://dx.doi.org/10.1017/S0022112086000149.

[60] B. Maneshian, K. Javadi, M.T. Rahni, R. Miller, Droplet dynamics in rotating flows, Adv. Colloid Interface Sci. 236 (2016) 63–82, http://dx.doi.org/10.1016/j.cis.2016.07.005.

[61] S. Chandrasekhar, The stability of a rotating liquid drop, Proc. R. Soc. Lond. A. Math. Phys. Sci. 286 (1404) (1965) 1–26, http://dx.doi.org/10.1098/rspa.1965.0127.

[62] R. Brown, L. Scriven, The shape and stability of rotating liquid drops, Proc. R. Soc. Lond. A Math. Phys. Sci. 371 (1746) (1980) 331–357, http://dx.doi.org/10.1098/rspa.1980.0084.

[63] W.-H.B. Wong, M.A. Hulsen, P.D. Anderson, A numerical model for the development of the morphology of disperse blends in complex flow, Rheol. Acta 58 (2019) 79–95, http://dx.doi.org/10.1007/s00397-018-01126-8.

[64] G.W.M. Peters, S. Hansen, H.E.H. Meijer, Constitutive modeling of dispersive mixtures, J. Rheol. 45 (2001) 659–689, http://dx.doi.org/10.1122/1.1366714.

[65] R. Poole, On the use of the Astarita flow field for viscoelastic fluids to develop a generalised Newtonian fluid model incorporating flow type (GNFFTy), J. Fluid Mech. 987 (2024) A2, http://dx.doi.org/10.1017/jfm.2024.344.

[66] G. Mompean, R. Thompson, P.S. Mendes, A general transformation procedure for differential viscoelastic models, J. Non-Newton. Fluid Mech. 111 (2–3) (2003) 151–174, http://dx.doi.org/10.1016/S0377-0257(03)00042-9.

[67] R.L. Thompson, P.R.S. Mendes, Considerations on kinematic flow classification criteria, J. Non-Newton. Fluid Mech. 128 (2–3) (2005) 109–115, http://dx.doi.org/10.1016/j.jnnfm.2005.04.002.

[68] R.L. Thompson, P.R. Souza Mendes, Persistence of straining and flow classification, Internat. J. Engrg. Sci. 43 (1–2) (2005) 79–105, http://dx.doi.org/10.1016/j.ijengsci.2004.07.011.

[69] R.S. Martins, A.S. Pereira, G. Mompean, L. Thais, R.L. Thompson, An objective perspective for classic flow classification criteria, Comptes Rendus Mec. 344 (1) (2016) 52–59, http://dx.doi.org/10.1016/j.crme.2015.08.002.

[70] P.J. Oliveira, A shear and elongational decomposition approach of the rate-of-deformation tensor for non-Newtonian flows with mixed kinematics, J. Fluid Mech. 1001 (2024) A17, http://dx.doi.org/10.1017/jfm.2024.1084.

[71] P.J. Oliveira, R.J. Poole, A new flow-type measure based on the triple decomposition method–application to two-dimensional flows, J. Non-Newton. Fluid Mech. 349 (2026) 105594, http://dx.doi.org/10.1016/j.jnnfm.2026.105594.

[72] B.D. Favis, J.-P. Chalifoux, The effect of viscosity ratio on the morphology of polypropylene/polycarbonate blends during processing, Polym. Eng. Sci. 27 (1987) 1591–1600, http://dx.doi.org/10.1002/pen.760272105.

[73] B. Favis, D. Therrien, Factors influencing structure formation and phase size in an immiscible polymer blend of polycarbonate and polypropylene prepared by twin-screw extrusion, Polymer 32 (1991) 1474–1481, http://dx.doi.org/10.1016/0032-3861(91)90429-M.

[74] V. Everaert, L. Aerts, G. Groeninckx, Phase morphology development in immiscible PP/(PS/PPE) blends influence of the melt-viscosity ratio and blend composition, Polymer 40 (1999) 6627–6644, http://dx.doi.org/10.1016/S0032-3861(99)00048-8.

[75] M. Villone, F. Greco, M. Hulsen, P. Maffettone, Simulations of an elastic particle in Newtonian and viscoelastic fluids subjected to confined shear flow, J. Non-Newton. Fluid Mech. 210 (2014) 47–55, http://dx.doi.org/10.1016/j.jnnfm.2014.05.003.

[76] S. Popinet, An accurate adaptive solver for surface-tension-driven interfacial flows, J. Comput. Phys. 228 (2009) 5838–5866, http://dx.doi.org/10.1016/j.jcp.2009.04.042.

[77] G. Esposito, Y. Dimakopoulos, J. Tsamopoulos, Buoyancy induced motion of a Newtonian drop in elastoviscoplastic materials, J. Rheol. 68 (2024) 815–835, http://dx.doi.org/10.1122/8.0000883.

[78] S. Popinet, A quadtree-adaptive multigrid solver for the serre–green–naghdi equations, J. Comput. Phys. 302 (2015) 336–358, http://dx.doi.org/10.1016/j.jcp.2015.09.009.

[79] D.L. Brown, R. Cortez, M.L. Minion, Accurate projection methods for the incompressible Navier–Stokes equations, J. Comput. Phys. 168 (2001) 464–499, http://dx.doi.org/10.1006/jcph.2001.6715.